

**Superconducting Properties of $(\text{MnFe}_2\text{O}_4)_x/\text{CuTl-1223}$
Composites**



By

Rashid Khan

(307-FBAS/MSPHY/F14)

Supervisor:

Dr. Muhammad Mumtaz

Assistant Professor
Department of Physics, FBAS,
IIU, Islamabad

**Department of Physics
Faculty of Basic and Applied Sciences
International Islamic University, Islamabad
(2016)**



Accession No

TH17296 ^{1/16}

TH17296

621-31042

RAS

Electric contacts

Nanoparticles-

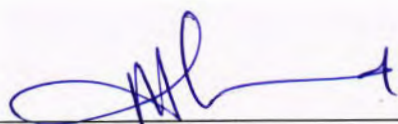
X-ray diffraction

Superconducting Properties of $(\text{MnFe}_2\text{O}_4)_x/\text{CuTi-1223}$ Composites

by:

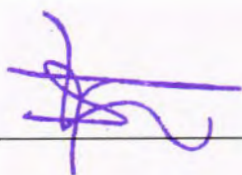
Rashid Khan
(307-FBAS/MSPHY/F14)

This Thesis submitted to Department of Physics International Islamic University,
Islamabad, for the award of degree of MS Physics.



CHAIRMAN
DEPT. OF PHYSICS
International Islamic University
Islamabad

Chairman Department of Physics
International Islamic University, Islamabad.

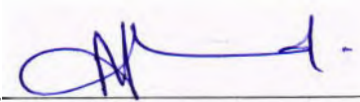


Dean Faculty of Basic and Applied Sciences
International Islamic University, Islamabad.


Final Approval

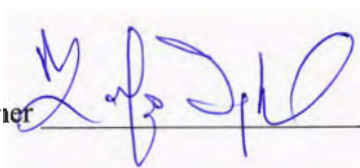
It is certified that the work presented in this thesis entitled “Superconducting properties of $(\text{MnFe}_2\text{O}_4)/\text{CuTi-1223}$ composites” by Rashid Khan Registration No. 307-FBAS/MSPHY/F14 fulfills the requirement for the award of degree of MS Physics from Department of Physics, FBAS, International Islamic University, Islamabad, Pakistan.

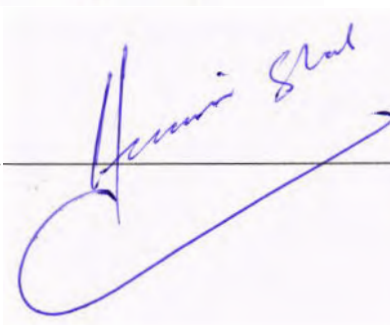
Viva Voce Committee

Chairman 

(Department of Physics)

Supervisor 

External Examiner 

Internal Examiner 

بِسْمِ اللَّهِ الرَّحْمَنِ الرَّحِيمِ

DEDICATED
To
Martyrs of APS
Peshawar

Declaration of Originality

I, **Rashid Khan** Registration No. 307-FBAS/MSPHY/F14 student of MS Physics (Session 2014-2016), hereby declare that the work presented in the thesis entitled “**Superconducting Properties of $(\text{MnFe}_2\text{O}_4)_x/\text{CuTi-1223}$ Composites**” in partial fulfillment of MS degree in Physics from International Islamic University, Islamabad, is my own work and has not been published or submitted as research work or thesis in any form in any other university or institute in Pakistan or abroad.



Rashid Khan
(307-FBAS/MSPHY/F14)

Dated: 26/12/2016

Forwarding Sheet by Research Supervisor

The thesis entitled “Superconducting Properties of $(\text{MnFe}_2\text{O}_4)_x/\text{CuTi-1223}$ Composites” submitted by **Rashid Khan** (Registration No. 307-FBAS/MSPHY/F14) in partial fulfillment of MS degree in Physics has been completed under my guidance and supervision. I am satisfied with the quality of his research work and allow him to submit this thesis for further process to graduate with Master of Science degree from Department of Physics, as per International Islamic University, Islamabad rules and regulations.



Dr. Muhammad Mumtaz

Assistant Professor
Department of Physics,
International Islamic University,
Islamabad.

Dated: 26/12/2016

Acknowledgement

All the praises to Almighty ALLAH, the most merciful and the sovereign power, who made me able to accomplish this research work successfully. I offer my humblest and sincere words of thanks to his Holy Prophet Muhammad (P.B.U.H) who is forever a source of guidance and knowledge for humanity. This work would have not been possible without the invaluable contributions of many individuals. First and foremost, I wish to thank my supervisor **Dr. Muhammad Mumtaz**, for all of his support, advice, and guidance during the whole period of my study. I would like to pay lot of appreciation to all my teachers who blessed me with knowledge and guidance.

I cannot forget the cooperation of my group members **Muhammad Waqas Rabbani, Abdul Jabar Bhutta, Liaqat Ali, Irfan Qasim, Waqee-ur-Rehman**, and specially **Muhammad Touqeer, Fahad Ali Shah, Yasir Mehmood Khan** and others who facilitated my research work.

Last but not the least I am highly indebted to my **family**, their continuous support, positive attitude and encouragement greatly motivated me throughout my educational career. They prayed for me, shared the burdens and made sure that I sailed through smoothly. I thank again ALMIGHTY ALLAH, who listens and responds to my every prayer.

Rashid Khan

Table of Contents

Chapter 1: Introduction.....	1
1.1 Superconductivity.....	1
1.2 Superconductivity Historical Review.....	2
1.3 Meissner effect.....	3
1.4 Classification of superconductors.....	5
1.4.1 Type-I superconductors.....	5
1.4.2 Type-II superconductors.....	6
1.5 Critical parameters of superconductors.....	7
1.5.1 Critical temperature.....	7
1.5.2 Critical Magnetic field.....	8
1.5.3 Critical current density.....	8
1.5.4 Correlation of three critical parameters.....	9
1.6 BCS Theory.....	10
1.7 Nanoscience and nanotechnology.....	11
1.8 Nanoparticles.....	12
1.9 Ferrites.....	13
1.9.1 Soft ferrites.....	13
1.9.2 Hard ferrites.....	14
1.10 Types of ferrites.....	14
1.10.1 Spinal ferrites.....	14
1.10.2 Tetrahedral sites.....	15
1.10.3 Octahedral sites.....	16
1.11 Classification of spinal ferrites.....	17
1.11.1 Normal spinal ferrites.....	17
1.11.2 Inverse spinal ferrites.....	17

1.11.3 Mixed spinal ferrites.....	17
1.12 Copper thallium based superconductor.....	18
1.13 Aims and objectives of research.....	18
References.....	19
Chapter 2: Literature Review.....	22
2.1. Literature review of superconducting composites.....	22
References.....	29
Chapter 3: Synthesis and Characterization Techniques.....	31
3.1 Nanoparticles synthesis.....	31
3.1.1 MnFe ₂ O ₄ nanoparticles synthesis.....	32
3.1.2 Synthesis of Cu _{0.5} Ba ₂ Ca ₂ Cu ₃ O _{10-δ} precursor.....	33
3.1.3 Synthesis of (MnFe ₂ O ₄) _x /CuTl-1223 nanoparticles superconductor composite.....	34
3.2 Experimental characterization techniques.....	35
3.2.1 X-rays diffraction (XRD).....	35
3.2.1.1 Basic principle.....	35
3.2.1.2 Bragg's law.....	36
3.2.1.3 Powdered diffraction method.....	37
3.2.1.4 Different parts of X-rays diffractometer.....	37
3.2.1.5 Major application of XRD.....	38
3.2.2 Scanning electron microscope (SEM).....	39
3.2.2.1 Different parts of SEM.....	40
3.2.2.2 Energy dispersive X-rays analysis (EDX).....	42
3.2.3 Four-probe method used for resistivity measurements.....	42
3.2.4 Fourier transform infrared FTIR spectroscopy.....	44
References.....	46
Chapter 4: Results and Discussion.....	47
4.1 X-Ray diffraction analysis.....	48
4.2 Scanning electron microscopy (SEM).....	52

4.3 Energy dispersive X-rays spectroscopy(EDX).....	53
4.4 Fourier transform infrared spectroscopy (FTIR).....	55
4.5 Resistivity measurements.....	57
Conclusions.....	59
References.....	60

List of Figures

Fig. 1.1: The superconductivity in Hg as discovered by Gills Holst and H. Kamerlingh Onnes in 1911.....	1
Fig. 1.2: Chronological discovery of higher critical temperature superconductors with time.....	3
Fig. 1.3: Meissner effect visual illustration.....	4
Fig. 1.4: Type-I superconductor response to applied magnetic field.....	5
Fig. 1.5: Type-II superconductor response to applied magnetic field.....	6
Fig. 1.6: Superconductors critical temperature illustration.....	7
Fig. 1.7: Difference between type-I and type-II superconductors.....	8
Fig. 1.8: Schematic representation of critical current density.....	9
Fig. 1.9: Critical phase diagram (Co-relation of T_c , H_c and J_c).....	10
Fig. 1.10: Cooper pair model.....	11
Fig. 1.11: Branches of nanoscience with other discipline of science.....	12
Fig. 1.12: A unit cell of spinal ferrites.....	15
Fig. 1.13: Illustration of Tetrahedral sites.....	16
Fig. 1.14: Illustration of octahedral sites.....	16
Fig. 1.15: Crystal structure of CuTl-1223.....	18
Fig. 3.1: Systematic diagram of physical and chemical methods for nanoparticles synthesis.....	31
Fig.3.2: Flow chart of Manganese ferrite nanoparticle synthesis.....	32
Fig. 3.3: Schematic flow chart of synthesis of $Cu_{0.5}Ba_2Ca_2Cu_3O_{10-\delta}$ precursor.....	33
Fig. 3.4: Schematic diagram of $(MnFe_2O_4)_x/CuTl-1223$ nanoparticle superconductor composite.....	34
Fig. 3.5: Working mechanism of XRD.....	36
Fig.3.6: Diffraction of X-rays from crystal planes.....	37
Fig. 3.7: Labeled diagram of X-ray diffractometer.....	38
Fig. 3.8: Labeled diagram of scanning electron microscope (SEM).....	39
Fig. 3.9: Schematic diagram of scanning electron microscope.....	41
Fig. 3.10: Schematic Labeled diagram of four probe apparatus (R-T measurements).....	43
Fig. 3.11: Working principle of FTIR absorption spectrum.....	44
Fig. 3.10: Modern FTIR apparatus.....	45
Fig. 4.1: XRD pattern of $MnFe_2O_4$ nanoparticles.....	48

Fig. 4.2: (a) XRD spectra of $(\text{MnFe}_2\text{O}_4)_x/(\text{CuTi-1223})$ superconductor composites with $x = 0$ wt. %.....	49
Fig. 4.2: (b) XRD spectra of $(\text{MnFe}_2\text{O}_4)_x/(\text{CuTi-1223})$ superconductor composites with $x = 0.5$ wt. %.....	50
Fig. 4.2: (c) XRD spectra of $(\text{MnFe}_2\text{O}_4)_x/(\text{CuTi-1223})$ superconductor composites with $x = 1.0$ wt. %.....	50
Fig. 4.2: (d) XRD spectra of $(\text{MnFe}_2\text{O}_4)_x/(\text{CuTi-1223})$ superconductor composites with $x = 1.5$ wt. %.....	51
Fig. 4.2: (e) XRD spectra of $(\text{MnFe}_2\text{O}_4)_x/(\text{CuTi-1223})$ superconductor composites with $x = 2.0$ wt. %.....	51
Fig. 4.3: Scanning electron microscopy (SEM) of $(\text{MnFe}_2\text{O}_4)_x/\text{CuTi-1223}$ composites with (a) $x = 0$, (b) $x = 0.5$ wt. %, (c) $x = 1$ wt. %, (d) $x = 1.5$ wt. % and (e) $x = 2.0$ wt. %.....	52
Fig. 4.4: EDX spectra of $(\text{MnFe}_2\text{O}_4)_x/(\text{CuTi-1223})$ superconductor composites with $x = 0$ wt. % and $x = 0.5$ wt. %.....	54
Fig. 4.5: (a) Unit cell of CuTi-1223.....	55
Fig. 4.5: (b) FTIR absorption spectra of $(\text{MnFe}_2\text{O}_4)_x/\text{CuTi-1223}$ superconductor composites with $x = 0, 0.5, 1.5$ and 2.0 wt. %.....	56
Fig. 4.6: Resistivity vs temperature measurements of $(\text{MnFe}_2\text{O}_4)_x/\text{CuTi-1223}$ superconductor composite samples with $x = 0, 0.5, 1.5$ and 2.0 wt. %.....	57

Abstract

Manganese ferrite (MnFe_2O_4) nanoparticles and $\text{Cu}_{0.5}\text{Tl}_{0.5}\text{Ba}_2\text{Ca}_2\text{Cu}_3\text{O}_{10-\delta}$ (CuTl-1223) superconductor were synthesized by sol-gel and solid-state reaction, respectively. Appropriate amount of MnFe_2O_4 nanoparticles were added to CuTl-1223 superconducting phase to obtain $\{(\text{MnFe}_2\text{O}_4)_x/\text{CuTl-1223}\}$; ($x = 0\sim 2$ wt.%) nanoparticles-superconductor composites. These composites were characterized by X-ray diffraction (XRD), Scanning electron microscopy (SEM), Fourier transform infrared (FTIR) absorption spectroscopy and (R-T) measurements. The tetragonal and spinal structure of CuTl-1223 superconducting phase and MnFe_2O_4 nanoparticles were verified by XRD analysis. The result of XRD analysis revealed that inclusion of MnFe_2O_4 nanoparticles doesn't disturb the crystal structure and stoichiometry of host CuTl-1223 superconducting phase. SEM images indicated that inter-grain weak-links of CuTl-1223 phase have been improved after addition of MnFe_2O_4 nanoparticles due to which density of voids and pores has been reduced. FTIR study revealed that MnFe_2O_4 nanoparticles do not substitute any constituent atoms of unit cell of host matrix and occupy the available inter-granular spaces. In resistivity versus temperature measurements decrease in T_c^{onset} (K) may be attributed to spin-charge reflection and trapping of charge carrier's due to the presence of MnFe_2O_4 nanoparticles at the grain-boundaries of CuTl-1223 superconducting phase.

Chapter 1: Introduction

1.1 Superconductivity

The phenomena of superconductivity deals with complete disappearance of material resistivity below a specific low temperature. This specific temperature conventionally termed as critical temperature and labelled as T_c . All those elements and compounds, which exhibits the phenomena of superconductivity at their specific critical temperatures, are called superconductors [1]. The materials like Pb, Nb, V_3Si , Nb_3Ge , $YBa_2Cu_3O_7$ and $TlSrBaCuO$ etc., are the few examples of superconducting materials.

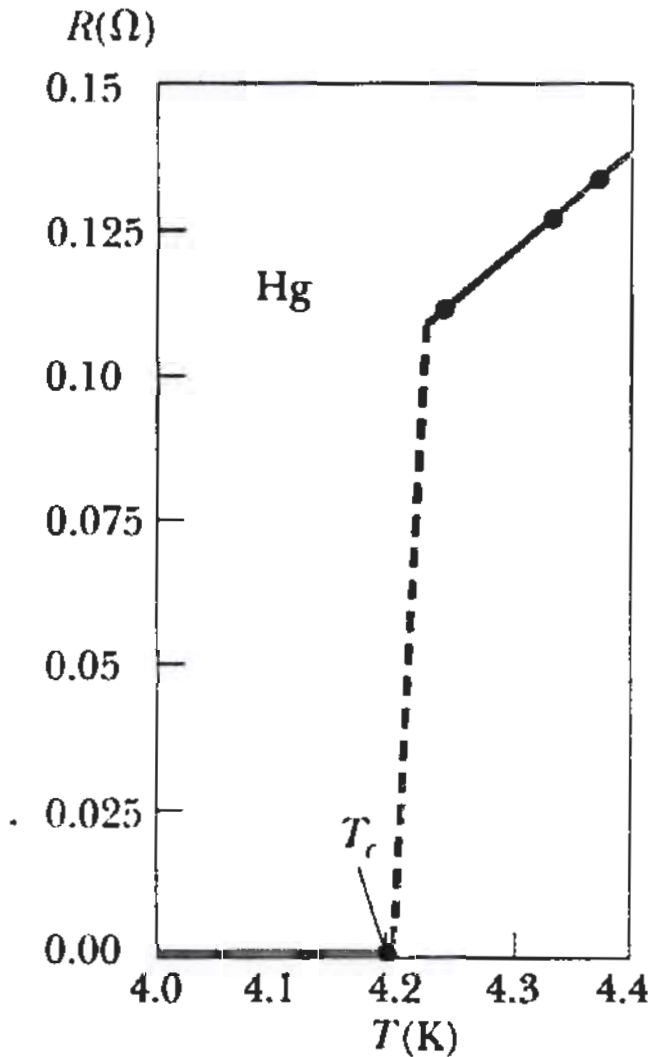


Fig 1.1: The superconductivity in Hg at 4.2 K as discovered by H. K. Onnes[2].

1.2 Superconductivity Historical Review

Phenomena of superconductivity was discovered by the H. Kamerlingh Onnes the Dutch Physicist in 1911, when he noticed the abrupt disappearance of the mercury electrical resistance at -269°C or 4K [3]. The Meissner and Robert Ochsenfeld were discovered the diamagnetic behavior of superconductors' materials. In their observation they observed that, the magnetic field lines are excluded by the superconducting material below a specific critical temperature T_c and on the bases of their observation they describe the relationship between the superconductivity and magnetic field and this phenomenon is known as Meissner effect or perfect diamagnetism [4]. While to explaining the perfect diamagnetic behavior of superconducting material, the famous novel London theory was put forward by F. London and H. London [5]. According to this theory, for a temperature below critical temperature of a superconducting material the exclusion of magnetic field take place because of decreased in electromagnetic energy which, carried by superconducting currents.

In 1957 J. Barden, L. Coopers and R. Schrieffer presented there famous BCS theory in field of superconductivity [6,7]. This theory was found to be very helpful in explaining the unique behavior of superconductors. With the continuous progress made in research on superconductivity, (LBCO) superconductive behavior at 30 K was found in 1986 by Bednorz and Muller [8]. Then YBaCuO superconductors were introduced in 1987 with the critical temperature of 90 K [9]. The (BSCCO) family of superconductor with critical temperature of 110 K was introduced in 1988 [10]. As compared to all type of superconductors, the $\text{Cu}_{1-x}\text{Tl}_x\text{Ba}_2\text{Ca}_2\text{Cu}_3\text{O}_{10-\delta}$ (CuTl-1223) phase drew the great attention of scientific community toward itself due to its higher value of critical temperature and other batter superconducting parameters [11]. The Fig 1.2 demonstrate the development made with passage of time in discovery of new superconductors with higher critical temperatures.

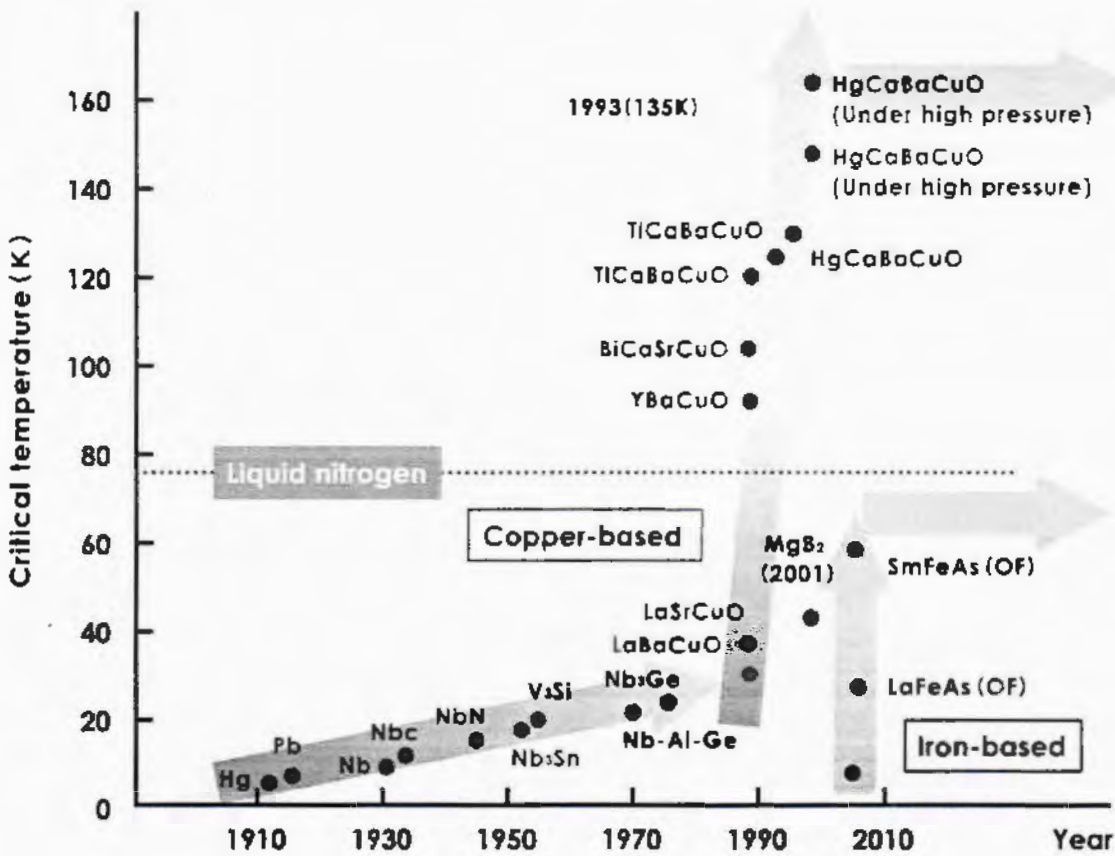


Fig 1.2: The discovery of higher T_c superconducting materials with time.

1.3 Meissner effect

A superconductor when placed in externally weak applied magnetic field H, allows the field lines penetration only for a short distance λ, also known as London penetration depth after which it decays quickly to zero. The effect where these magnetic lines are expelled from a superconducting specimen is known as Meissner effect, and it is a unique feature of superconductivity phenomena. The Fritz and Heinz London, are the two brothers who explained the Meissner effect and showed that, the minimized electromagnetic energy in a superconductor is given by

$$\Delta^2 H = \lambda^{-2} H \dots\dots\dots 1.1$$

Where H and λ are the magnetic field and London penetration depth respectively [12]. This equation is known as London equation and it anticipate that in a superconductor, the magnetic field decay exponentially from whatever initial value it has at the surface of superconductor.

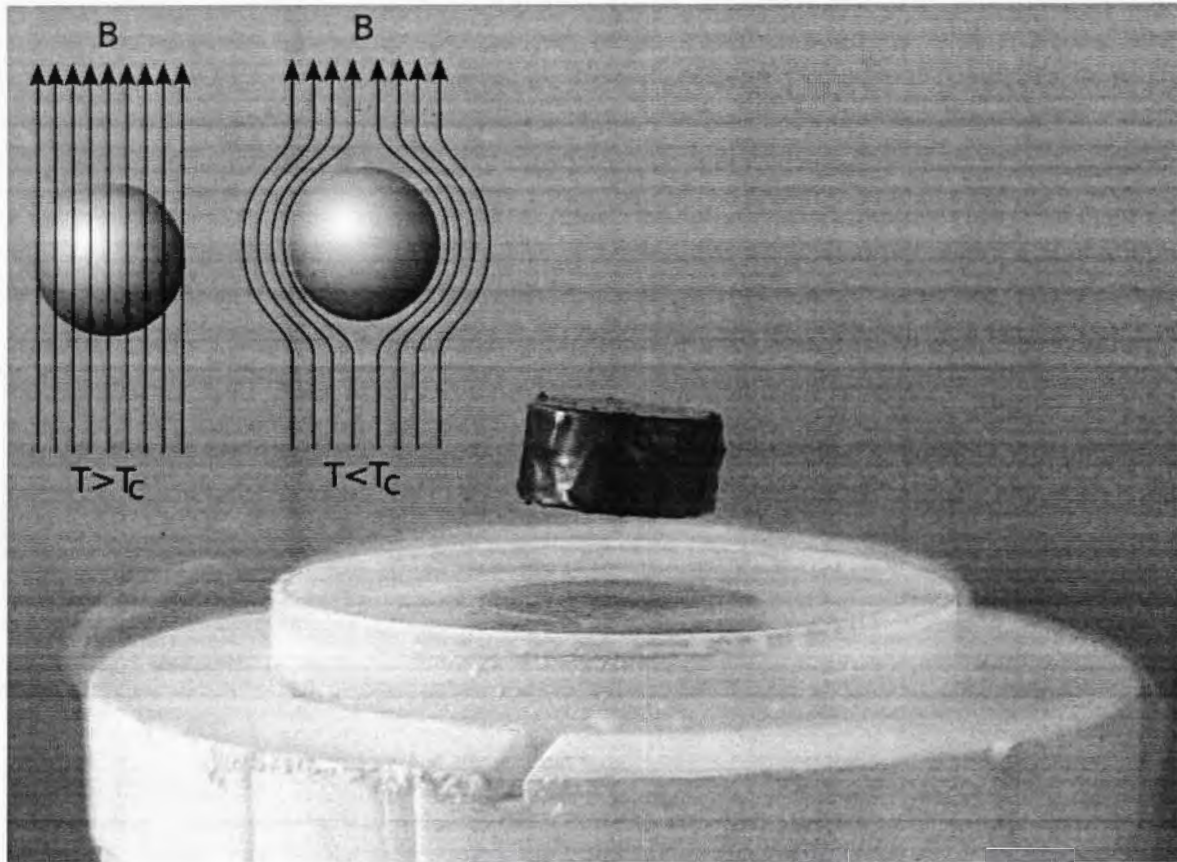


Fig 1.3: Meissner effect visual illustration [13].

When the externally magnetic field is too large then Meissner effect breaks down. The way in which this break down occurs divide the superconductors in two broad categories like type-I and type-II respectively. In type-I, as the magnitude of externally applied magnetic field exceed the critical value H_c , the superconductivity is suddenly destroyed. While in type-II superconductors, the partial penetration of flux lines take place as the applied field increased above the critical value H_{c1} and remained below H_{c2} . But in this state material still remained in superconducting state and offered zero resistance to the flow of electric current but not for the large values of current. By exceeding the upper critical field value H_{c2} , material lost its superconducting state and an abrupt change to normal state of material take place. The mixed state occurs mainly due to existence of

vortices in this state which allow penetration of external applied field lines, without affecting the superconducting state of material. Except (technetium, vanadium, niobium and carbon nanotubes) the majority of pure elemental superconductors are the type-I superconductors while nearly all the impure and compound superconductors are included in type-II superconductor category.

1.4 Classification of superconductors

Superconductor on the basis of their response to the external magnetic field are classified into two broad categories

1.4.1 Type-I superconductors

The least value of magnetic field below which the superconductor material exclude the external magnetic field is known as critical magnetic field and denoted by H_c . The mercury, tin, lead are the few examples of type-I superconductor having least value of critical magnetic field. Meissner effect is obeyed by the type-I superconductors and also shown in Fig 1.3, were it can be observed that beneath H_c , the external magnetic field is almost completely exclude and material is said to be in superconducting state and abrupt change to normal state take place after reaching H_c and external magnetic field penetrate inside the superconductor.

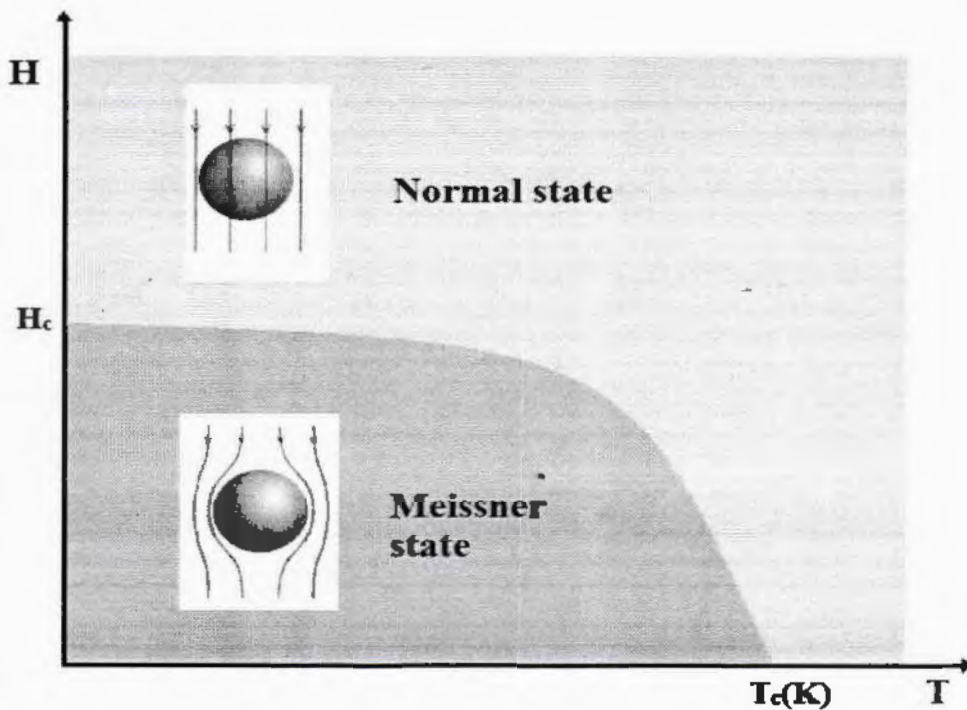


Fig 1.4: Type-I superconductor.

Type-I superconductors are also termed as soft superconductor. These superconductors are normally not capable of carrying high current and having minimum value of H_c , therefore they are not suitable for practical applications.

1.4.2 Type-II superconductors

In comparison between both type-I superconductors and type-II superconductors, it was found that the type-II superconductors don't have a property to lose their diamagnetic behavior instantly and shows paramagnetic response in corresponds to externally applied field as that of type-I superconductors shown in Fig 1.4. The three distinguishable states in Type-II superconductors are superconducting, mixed and normal state. These type of superconductors showing diamagnetic or superconducting behavior beneath H_{c1} while in the region between H_{c1} and H_{c2} , they partially allowed the magnetic field lines to penetrate inside the specimen in form of vortices and this region is known as mixed state or vortex state. Above the value of upper critical field H_{c2} , the specimen transformed to normal material and this region known as normal state.

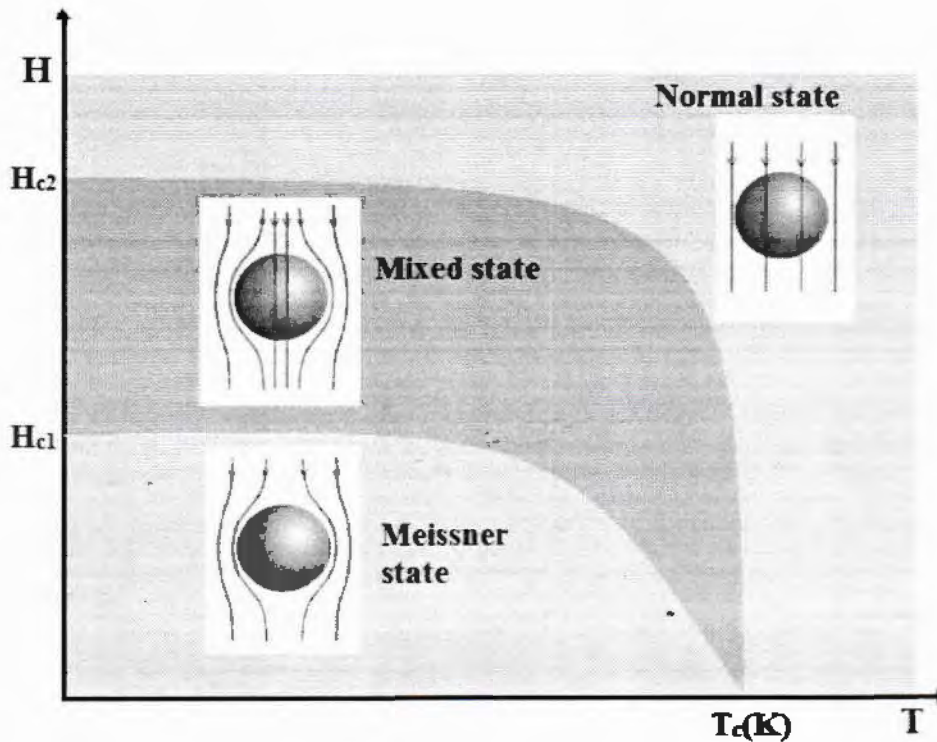


Fig 1.5: Type-II superconductor [14].

1.5 Critical parameters of superconductors

The three essential parameters in phenomena of superconductivity are T_c , J_c and H_c respectively. Moreover, we can explain phenomena of superconductivity based on these parameters.

1.5.1 Critical temperature (T_c)

For any superconducting material, the minimum temperature below which material resistivity completely disappear or vanish, referred as critical temperature of that material [15].

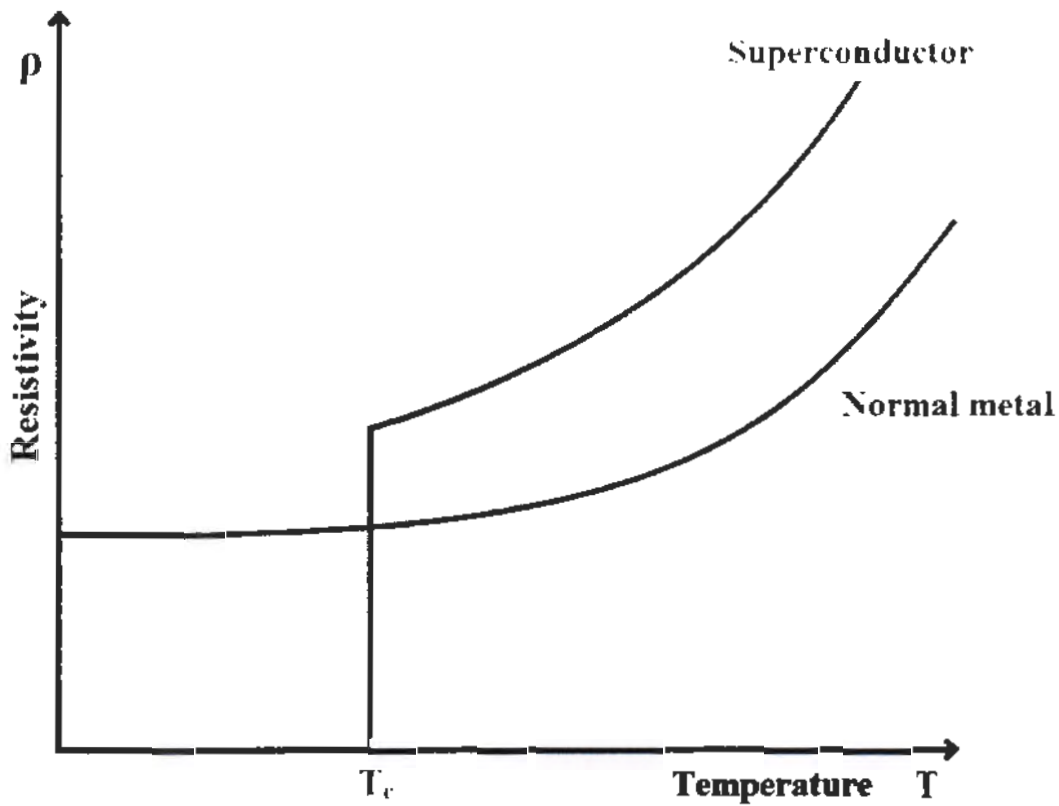


Fig 1.6: Superconductors critical temperature T_c .

1.5.2 Critical Magnetic field (H_c)

The uppermost value of magnetic field below which material sustain its superconducting state and above which it acts like normal material. Different states of superconducting materials can be represented by the correlation between T_c and H_c .

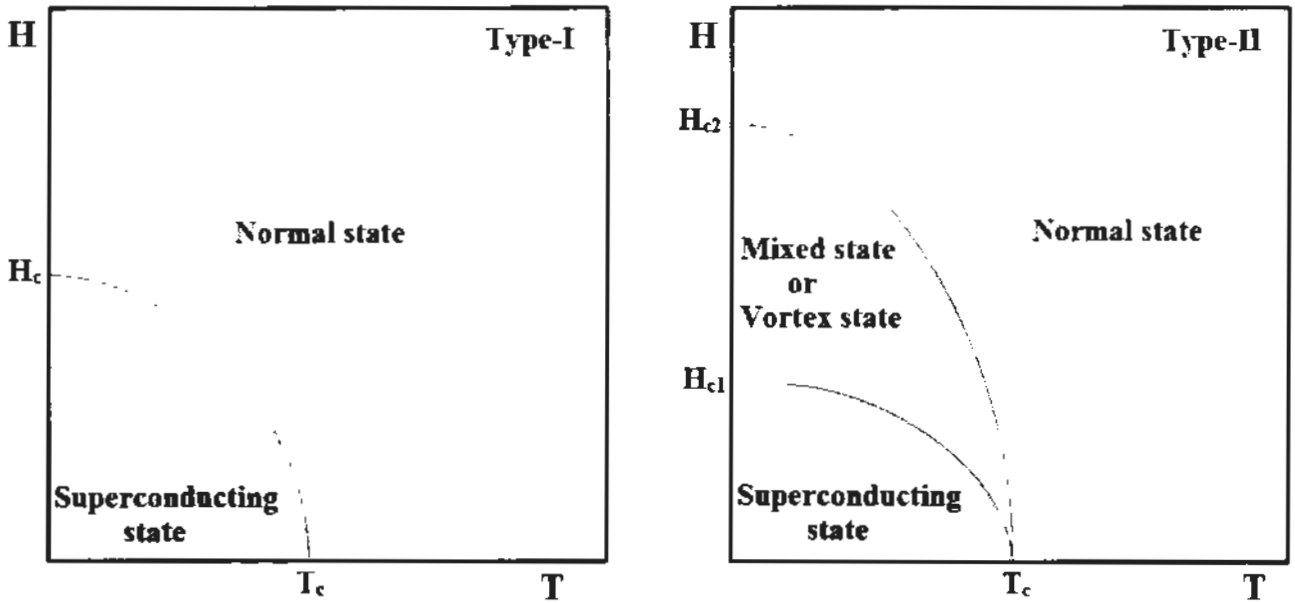


Fig 1.7: The magnetic field vs temperature.

1.5.3 Critical current density (J_c)

From practical point of view, an important parameter that decide suitability of a superconductor for practical application defined by its critical current density (J_c) [16]. It could be described as the maximum current which a superconductor can pass though it self in superconducting state.

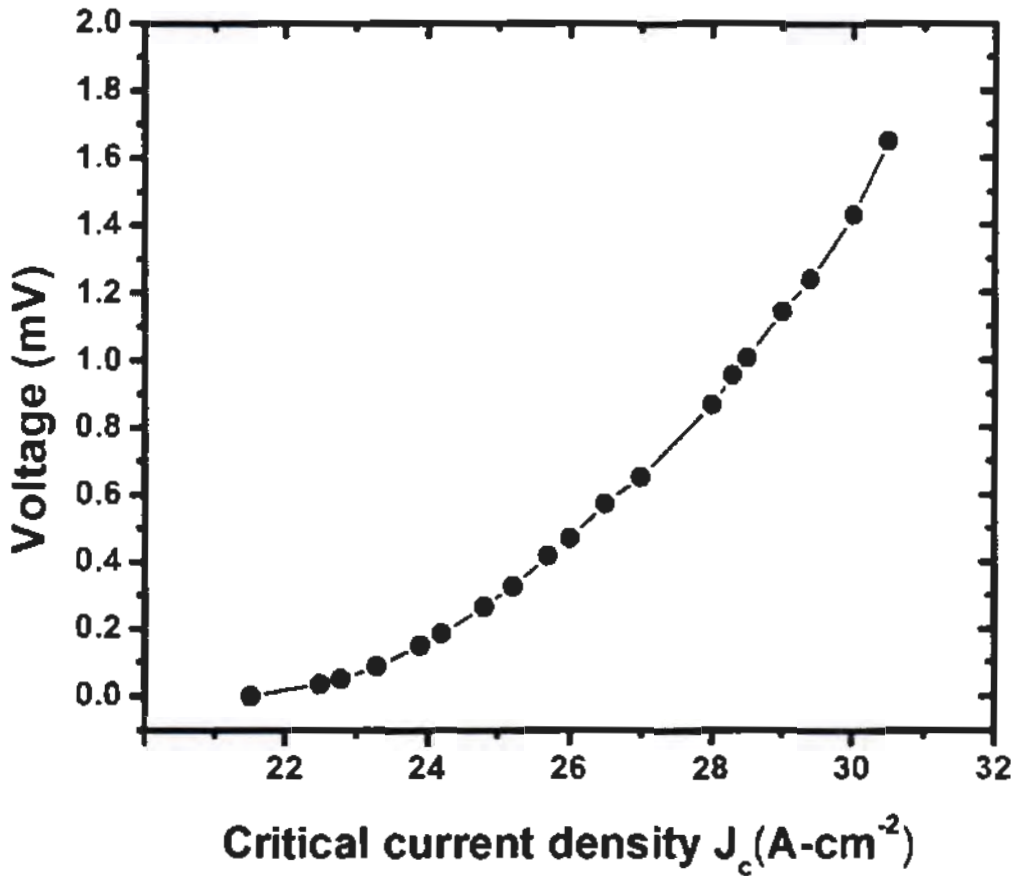


Fig 1.8: The characteristic I-V curve of superconductors.

1.5.4 Correlation of three critical parameters

All the critical parameters of a superconducting material correlated to each other as shown in Fig 1.8. The imaginary surface, which enclosed by these parameter exhibits the superconducting state of the material. It was found that, all critical parameters directly dependent on each other's and alteration or change in one may destroyed the superconducting state of the superconducting material [17].

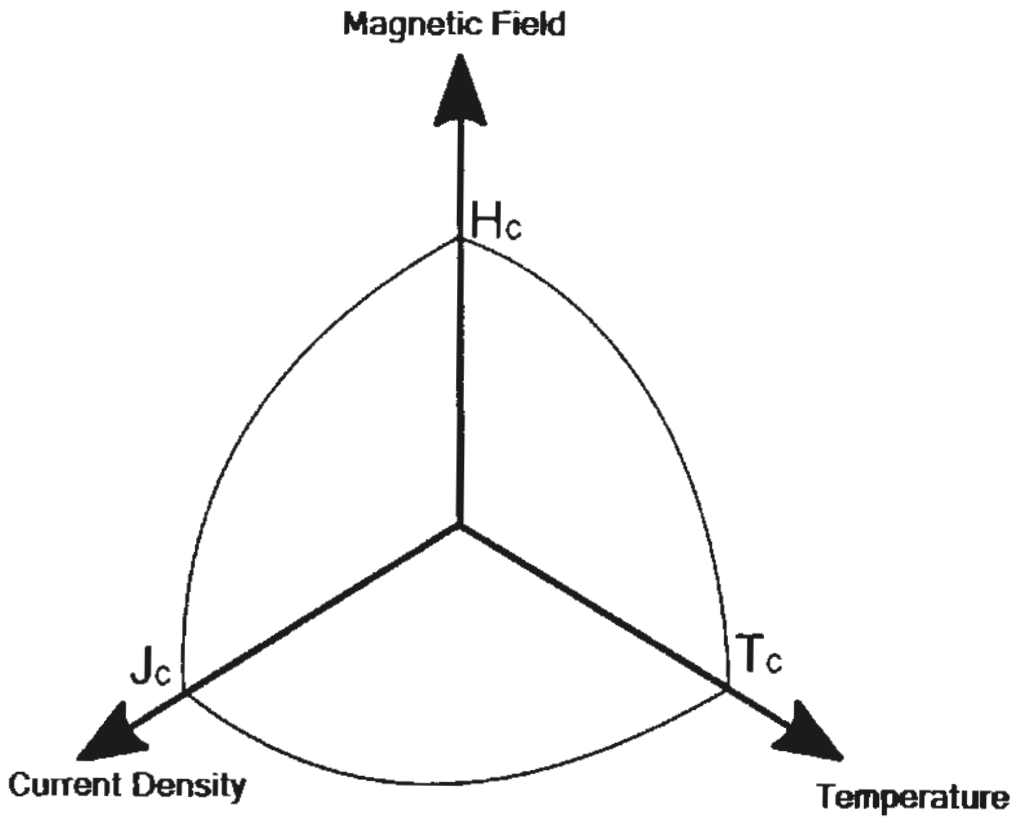


Fig 1.9: Critical phase diagram formed by the correlation of J_c , H_c and T_c [18].

1.6 BCS Theory

The well-known BCS theory was proposed in 1957 by three American physicists John Bardeen, John Robert Schrieffer and Leon Cooper [19]. This theory well explained the characteristics of type-I superconductors, but unable to describe the superconductivity phenomena in case of high temperature superconductors (HTSCs) and exotic superconductors. The mechanism of superconductivity is well explained in terms of electron pairs. These pairs are also known as Cooper pairs and shown in Fig. 1.9.

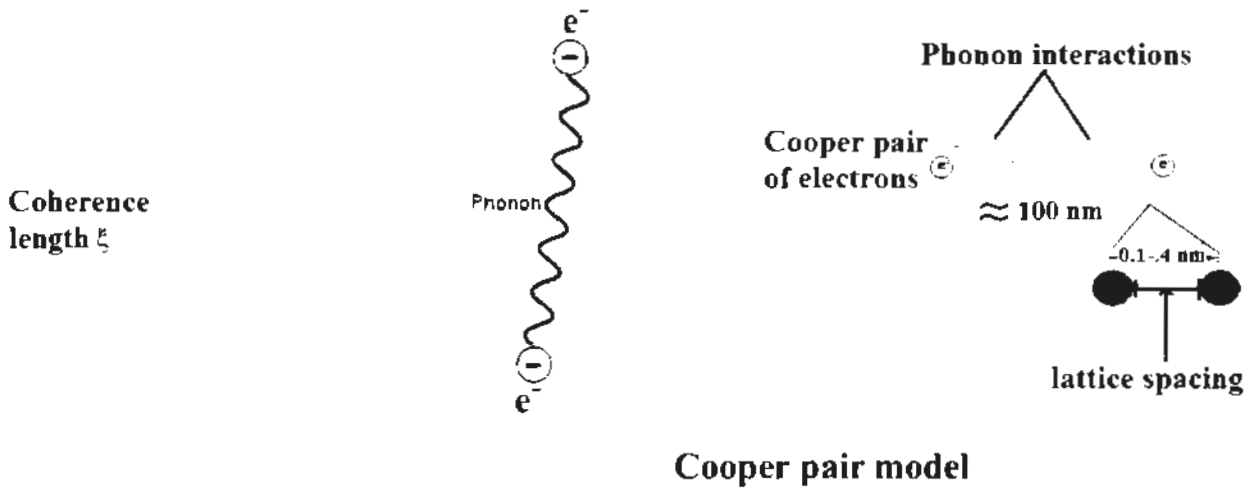


Fig 1.10: Schematic representation of cooper pair model.

The BCS theory explained the mechanism of pair formation and according to this theory when the interaction between electrons take place then it gives rise to coulomb attraction between them and then as a result they coupled together to formed a cooper pair. It was observed that, when total spin off a cooper pair is calculated then results shows zero spin. As we know that boson particles have zero spin, so we can assume the cooper pair as a simple boson particle. The observation shows that in a system having temperature less than critical temperature all these particles share the same lowest energy level and it is referred as bose condensation. And as a result of this condensation all particles showing same wave function.

1.7 Nanoscience and nanotechnology

Nanoscience deals with the brief study of materials at nanometer scale. The materials having at least one dimension in range of (1-100nm) are termed as nanomaterials. Nanoscience almost involved in all fields of applied sciences, where the basic aim is to organize the concerned material at nanoscale according to its practical application requirement. The observations show that most properties of nanomaterials are very different from its bulk counterpart. The most reasonable explanation of this prominent change in properties could be related to the increased in volume fraction as well as the quantum effects occurs as result of reduction in specimen size. Observations shows that as the size of bulk materials decreased, the proportion of atoms increased on the surface as compared to internal core of the material. The nanotechnology mostly deals with the synthesis and characterization of physical properties of nanomaterials and fabrication of nano-

scale devices through these materials. The correlation between different fields of science and nanoscience could be related to each other's as shown in Fig 1.11.

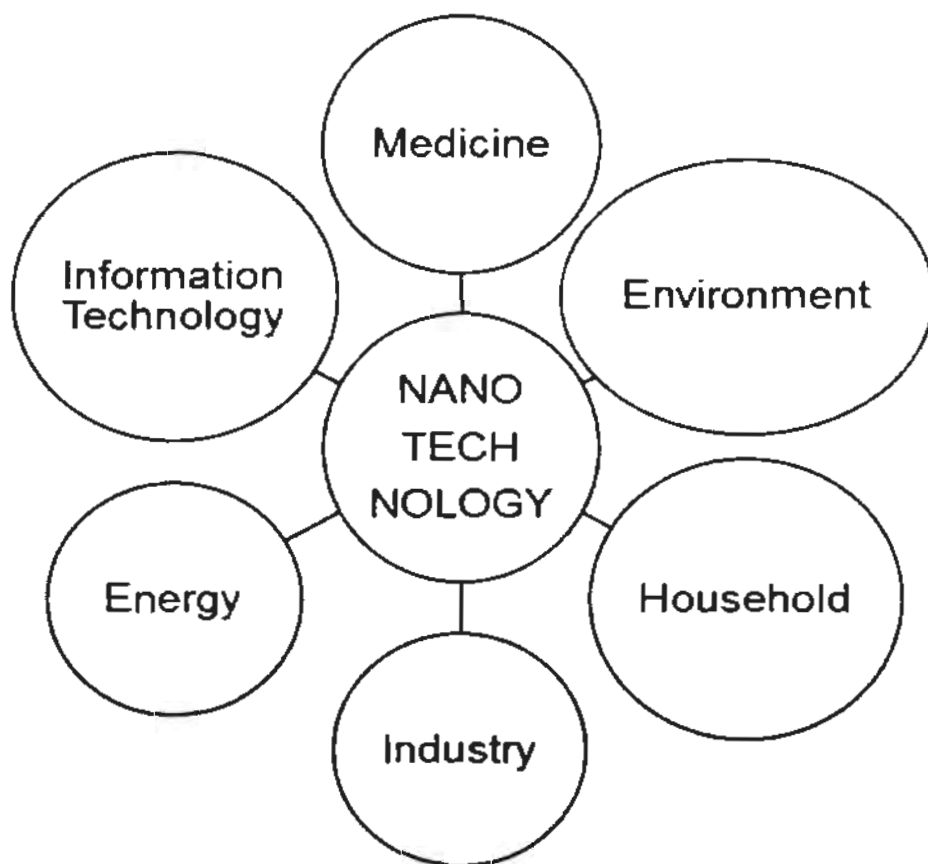


Fig 1.11: Nanoscience with other discipline of science.

As the degrees of surface reactivity of these nanomaterial is very high which most probably due to large surface to volume ratios, so consequently the nanotechnology also deals with the more challenging devices fabrication for various numbers of practical applications. In any technological application based on nanoparticles use, required to synthesize the nanoparticle with uniform chemical composition as well as mono-dispersion i.e. with no agglomeration.

1.8 Nanoparticles

Conventionally the particles having average diameter in range of (1-100 nm) are called nanoparticles. Unlike the bulk counterpart, the nanoparticles exhibit unusual characteristics at the scale of nanometer. For example, the ferroelectric and ferromagnetic material alters their bulk state properties when size of these materials brings down to nanometer range. Similarly, those materials

exhibit the semiconducting properties in the bulk form showing non-conducting properties as the size reduced up to nanometers range. Gold nanoparticles unveil the catalytic characteristic in dimension of nanometer. Decrease of imperfection, increase in surface to volume ratio, high surface energy as well as quantum or spatial confinement are the few well know reasons for alteration in properties caused by the reduction in specimen size [20-21].

1.9 Ferrites

The origin of word “Ferrite” is from Latin word used for iron. All those metal oxides having the iron as compulsory constituent are known as ferrites. Ferrites nanoparticles are basically showing magnetic nature and we placed them in the category of ceramic compounds. From the dielectric characteristics of ferrites, we can conclude that they allow the EM waves to pass through them. Ferrites have spinal structure. The $MOFe_2O_3$ is the most common general form conventionally used to represent ferrites and sometime also can be written as MFe_2O_4 , where M is any divalent element like zinc, magnesium, manganese, nickel etc. Some unique properties make them more suitable for numerous applications based on them. These properties include dielectric, magnetic, electric properties, which were utilized in number of ways for practical applications [22]. It is also observed that, at ordinary room temperature the normal state resistivity depends on chemical composition and the methods which were used during synthesis of ferrites [23]. Ferrites are further classified into two broad categories based on magnitude of demagnetization force required to demagnetize the given ferrite materials and they are given as follows;

1. Soft ferrites
2. Hard ferrites

1.9.1 Soft ferrites

The type of ferrites material having least value of coercivity as well as having narrow M-H loop are known as soft ferrites [24]. The lower coercivity of these materials implies that, we can demagnetize the material with the help of very small demagnetization force against its remanence. Mostly all those ferrites having coercivity in range of 1KA/m may also termed as soft ferrites. The main well known applications of soft ferrites include its use in transformer and the electromagnetics [25]. The Nickel-zinc ferrites and Magnesium-Zinc ferrite are the two example of soft ferrites. The existence of Zn influenced the magnetic properties of these mixed ferrites. .

1.9.2 Hard ferrites

The hard ferrites were discovered in 1950. As compared to soft ferrites, to demagnetize the given hard ferrite material we need large demagnetization force against its remanence. So it means that, these material exhibits larger coercivity than soft ferrites [26-28]. The permanent magnetic is one of the best example made up of such materials. Mostly for this type of materials, the value of coercivity is greater than 10KA/m. Some well know examples of ferrites include strontium ferrites, barium-ferrite, barium-strontium mixed ferrites, cobalt ferrite and alloys of cobalt etc. These materials are mostly used for fabrication of communication systems, tuning devices and phase shifter etc. Also the low-cost of ferrites make them more suitable in refrigerator sealing like applications.

1.10 Types of ferrites

The ferrites could be divided into three major types accordingly to their structure as follows;

1. Spinal ferrites
2. Hexagonal ferrites
3. Garnets

1.10.1 Spinal ferrites

In 1951, Nishikaw and Bragg first investigated the structure of spinel group [29-31]. The spinal ferrites are mostly designated by the formula MFe_2O_4 , Where M is representing the divalent metal ion like (Fe^{+2} , Zn^{+2} , Ni^{+2} , Co^{+2} , Mg^{+2} and Cd^{+2}) etc. Spinal ferrites are also known as by name of cubic ferrites. To understand the crystal structure of spinal ferrites we can divide its unit cell in to eight octants. The FCC lattice made by the combination of 32 oxygen ions and have two interstitial sites of different types and these sites are named as tetrahedral sites and octahedral sites respectively. The three dimensional arrangement of these two cubic structure formed the resultant spinal structure. The schematic representation of spinal structure is shown in Fig 1.12.

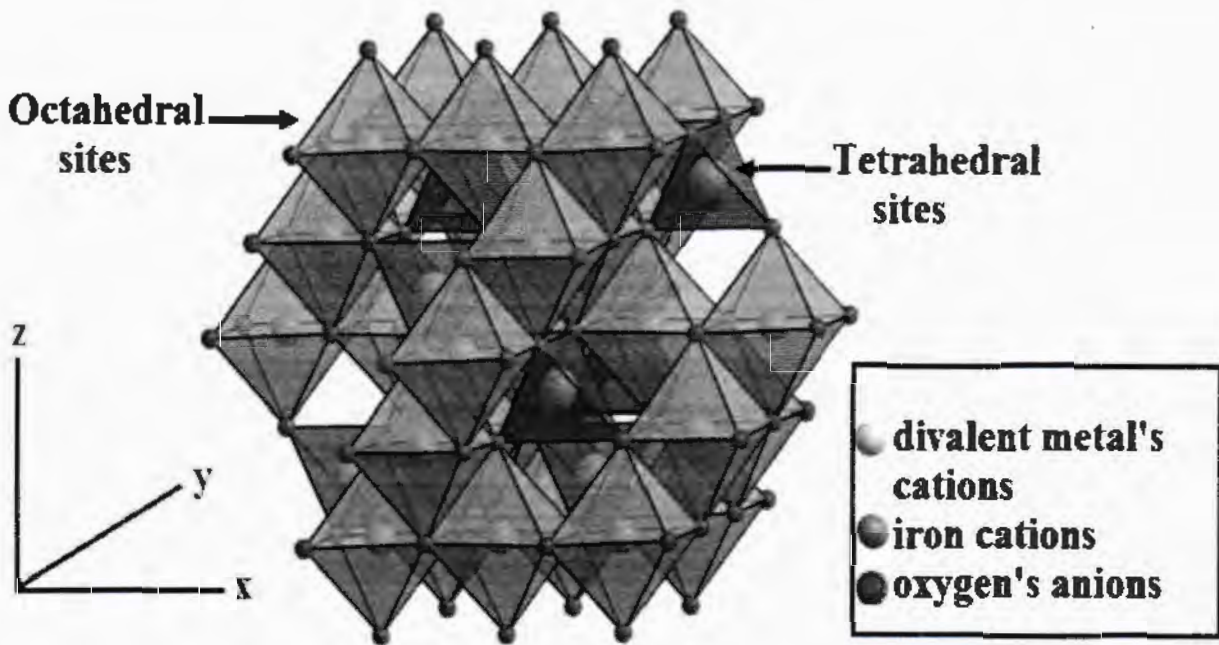


Fig 1.12: A unit cell of spinal ferrites [32].

A single unit cell of ferrite consists of 32 anions of oxygen, 8 cations of divalent metal and 16 trivalent cations of iron respectively. The $X_8Fe_{16}O_{32}$ give the spinal ferrite chemical composition, where $8*(XFe_2O_4)$ gives the total number of atoms/unit cell.

1.10.2 Tetrahedral sites

The tetrahedral sites actually consist of 4 oxygen anions with a single divalent metal cation [33]. The occupation of tetrahedral sites by these oxygen ions and the divalent metal cations is demonstrated in Fig 1.13. The four lattice oxygen atoms arranged in such a way that they formed the tetrahedral structure while the fifth interstitial atom lies at the center of this arrangement. The three atoms out of four in this arrangement touching each other in a same plane while fourth one remain at the apex position to them. In a unit cell total number of tetrahedral sites are 64 and only 8 of them are filled with cations.

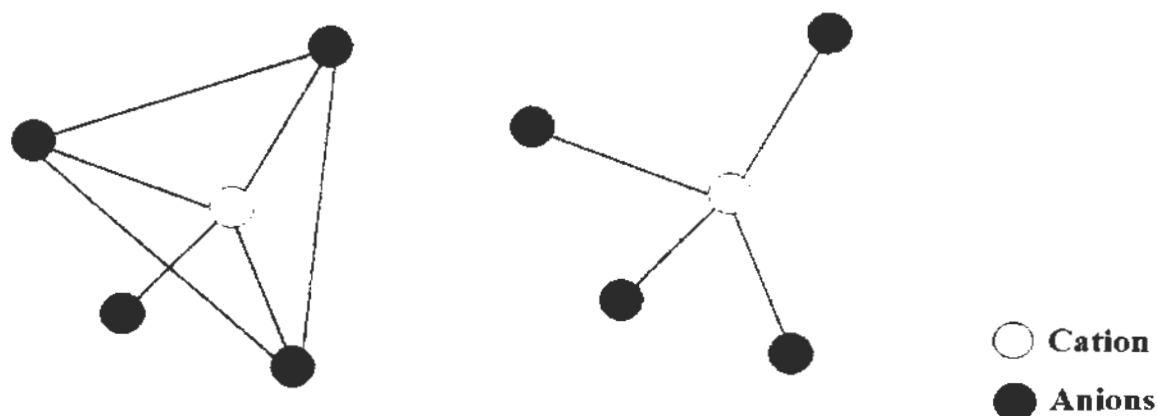


Fig 1.13: Illustration of Tetrahedral sites [34].

1.10.3 Octahedral sites

The octahedral sites are the combination of six anions and one trivalent cation or iron respectively [35]. The octahedral arrangement of these anions and cation is shown in Fig.1.14. The six oxygen anions surround the cation or interstitial atom in such a way that in octahedral arrangement the four atoms sharing the same while on other hand one is located above and one is located below to this plane. In a single unit cell of spinal structure have 32 available octahedral sites out of which 16 are occupied by cations.

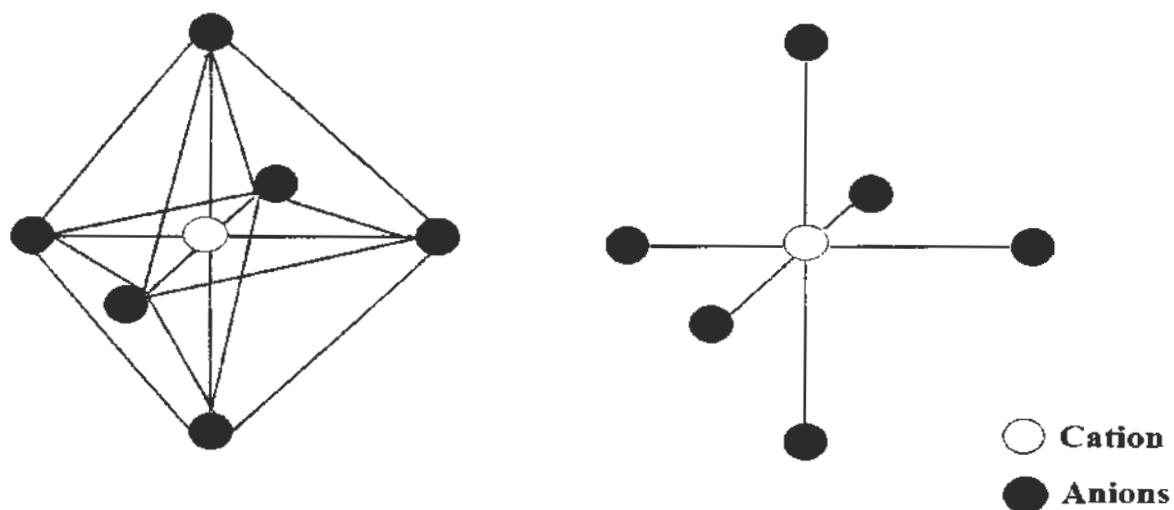


Fig 1.14: Illustration of octahedral sites [36].

1.11 classification of spinal ferrites

The classification of spinal ferrites is strongly based on the cations distribution between A site or B site, i.e. tetrahedral site and octahedral site respectively. The three well know classification of spinal ferrites are as follow;

1. Normal spinal ferrites
2. Inverse spinal ferrites
3. Mixed spinal ferrites

1.11.1 Normal spinal ferrites

The chemical composition of normal spinal ferrites can be written as $[T^{2+}]_A[R^{3+}]_B O_4$. In this type of ferrite, the divalent cation is strictly bound to reside on tetrahedral site and trivalent cation is strictly bound to reside on octahedral site only. The $ZnFe_2O_4$ is an excellent example where the Fe^{3+} cations occupy octahedral site and Zn^{2+} cation occupy the tetrahedral site only. The eight tetrahedral and sixteen octahedral site of a unit cell are all filled [37].

1.11.2 Inverse spinal ferrites

The $[R^{3+}]_A[T^{2+}R^{3+}]_B O_4$ is the chemical composition of invers spinal ferrites. The trivalent cations equally reside on both tetrahedral and octahedral sites. The $NiFe_2O_4$ is an example of such ferrites where almost 50% of trivalent cation reside on tetrahedral site or A and rest of 50% reside on the octahedral site or B. So the chemical composition of final compound can also be written as $[Fe^{3+}]_A[Ni^{2+}Fe^{3+}]_B O_4$ [38].

1.11.3 Mixed spinal ferrites

This type of spinal ferrites has the hybrid structure of previous two types i.e. the structure is in between the normal and invers spinal ferrites. The $[T^{2+\delta}R^{3+1-\delta}]_A[T^{2+1-\delta}R^{3+\delta}]_B O_4$. Where δ is termed as inversion parameter and in case of hybrid ferrites it is very useful in determining the structure of given hybrid ferrites. If δ is equal to one then the structure of given, hybrid ferrite is normal spinal ferrite and for δ equal to zero the structure is invers spinal ferrite. So it means that, inversion parameter values vary from 0-1. Therefor it means that, in these type of ferrites distribution of divalent and trivalent cations at A and B sites is not uniform or unequal [39].

1.12 Copper thallium based superconductor

$\text{CuBa}_2\text{Ca}_{n-1}\text{O}_{2n-1}\{\text{Cu-12}(n-1) \text{ n, n= 1, 2, 3...}\}$ exhibits the tetragonal structure and normally its synthesis required high pressure conditions. This superconductor has the higher value of critical current density as well as the critical temperature which about 120 K approximately. The new family of superconductors CuTl-1223 emerge when thallium is added to it. This new family have improved critical temperature about 132K and crystallographic structure of its unit cell is also shown in Fig. 1.15. The two division of this structure are superconducting block and the charge reservoir layer which actually acts as a source of charge carriers supply to the planes [40-42].

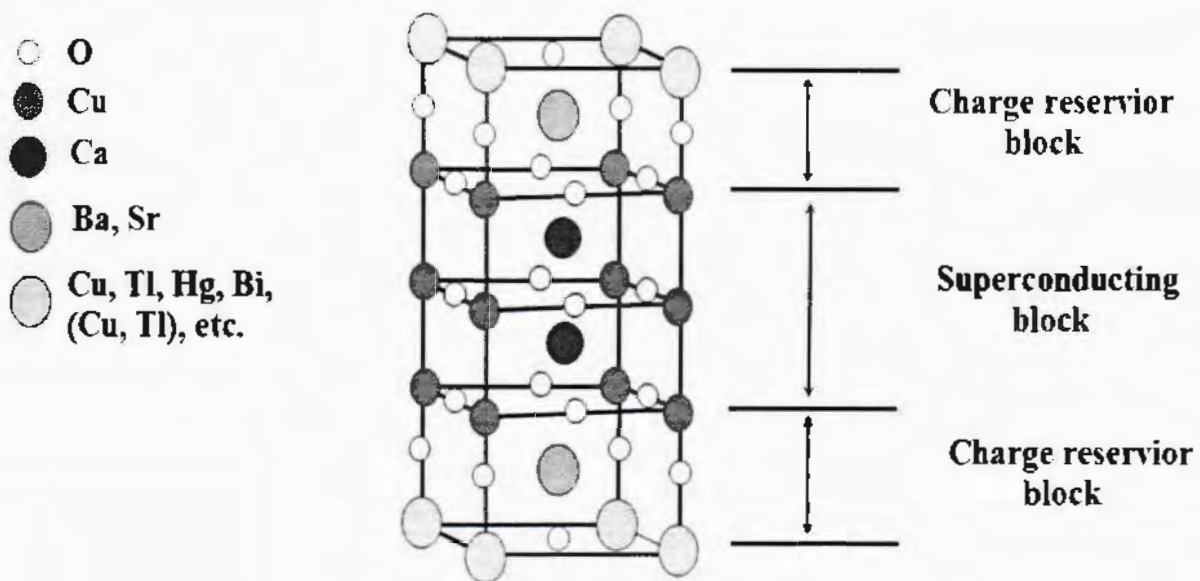


Fig 1.15: Unit cell of CuTl-1223.

1.13 The main objective of this research

1. To improve superconductivity by the inclusion nanoparticles at grain-boundaries.
2. To improve its critical parameters like (T_c , J_c , H_c).
3. Made it more suitable for various industrial applications.

References

- [1] M. Boerhaave, "History and significance of the discovery of superconductivity by Kamerlingh Onnes in 1911" *Physica C* **479** (2012) 30.
- [2] D. Delft, and Peter. Kes, "The discovery of superconductivity " *Phys. Today* **63** (2010) 38.
- [3] H. K. Onnes, "The resistance of pure mercury at helium temperatures" *Commun. Phys. Lab. Univ. Leiden.* **12** (1911) 1.
- [4] W. Meissner and R. Ochsenfeld, *Naturwissenschaften*, **21** (1933) 787.
- [5] F. and H. London. *Proceedings of the Royal Society of London*, **149** (1935) 71.
- [6] J. Bardeen, L. N. Cooper, and J. R. Schrieffer, "Microscopic theory of superconductivity" *Phys. Rev.* **106** (1957) 162.
- [7] J. Bardeen, L. N. Cooper, and J. R. Schrieffer, "Theory of superconductivity" *Phys. Rev.* **108** (1957) 1175.
- [8] Hardy, John R., and John W. Flocken, "Possible origins of high- T_c superconductivity." *Phys. Rev. Lett.* **60** (1988) 2191.
- [9] E. Babic, Z. Marohnic, M. Prester, and N. Brnicevic, "Variation with density of the transport properties of YBaCuO superconductors." *Philos. Mag. Lett.* **56** (1987) 91.
- [10] Maeda, Hiroshi, Yoshiaki Tanaka, Masao Fukutomi, and Toshihisa Asano, "A new high- T_c oxide superconductor without a rare earth element." *Jpn. J. Appl. Phys.* **27** (1988) 209.
- [11] J. Robert, Schrieffer, and James S. Brooks, "Handbook of high-temperature superconductivity" Springer Science (2007).
- [12] J. Bardeen, L. N. Cooper, and J. R. Schrieffer, "Theory of superconductivity" *Phys. Rev.* **108** (1957) 1175.
- [13] B. Rosenstein, and D. Li, "Ginzburg-Landau theory of type II superconductors in magnetic field" *Revi. Phys.* **82** (2010) 109.
- [14] B. Rosenstein, and D. Li, "Ginzburg-Landau theory of type II superconductors in magnetic field" *Revi. Phys.* **82** (2010) 109.

- [15] M. Ali. Omar, "Elementary solid state physics" Pearson Education India (1975).
- [16] N. Hosseini, S. Kananian, A. Zabetian, and M. Fardmanesh, "Point contact based method to measure critical current density of superconductor bulk" *Phys. Procedia* **36** (2012) 655.
- [17] H. Froehlich, "Theory of the superconducting state" *Phys. Rev.* **79** (1950) 845.
- [18] I. Zutic, J. Fabian, and S. D. Sarma, "Spintronics: Fundamentals and applications" *Rev. Phys.* **76** (2004) 323.
- [19] H. Froehlich, "Theory of the superconducting state " *Phys. Rev.* **79** (1950) 845.
- [20] L. L. Hench, and Jon K. West, The sol-gel process *Chem. Rev.* **90** (1990) 33.
- [21] R. Taylor, S. Coulombe, T. Otanicar, P. Phelan, A. Gunawan, W. Lv, G. Rosengarten, R. Prasher, and H. Tyagi, "Small particles, big impacts: A review of the diverse applications of nanofluids" *J. Appl. Phys.* **113** (2013) 11301.
- [22] R.S. Tebble and D.J. Craik, *Magnetic Materials*, John Wiley and Sons, New York, (1969).
- [23] J. Smit and H.P.J. Wijn "Ferrites" John Wiley and Sons New York (1959).
- [24] Eric Charles. Snelling, "Soft ferrites." (1969).
- [25] Martha. Pardavi-Horvath, "Microwave applications of soft ferrites" *J. Magn. Mater.* **215** (2000) 171.
- [26] H. Stablein, "Hard ferrites and plastoferrites" *Handbook of Ferromagnetic Materials* **3** (1982) 441.
- [27] Mitsuo. Sugimoto, "The past, present, and future of ferrites" *J. Am. Ceram. Soc.* **82** (1999) 269.
- [28] Fidler, Josef, Thomas Schrefl, Sabine Hoefinger, and Maciej Hajduga, "Recent developments in hard magnetic bulk materials" *J. Phys. Condens. Matter* **16** (2004) 455.
- [29] Alex. Goldman " Handbook of modern ferromagnetic materials" Springer Science & Business Media **505** (2012).
- [30] Kurt H. Jurgen. Buschow, " Handbook of magnetic materials" Elsevier **15** (2003).

- [31] V. A. M. Brabers, "Handbook of Magnetic Materials" Progress in spinel ferrite research **8** (1995).
- [32] Kurt E. Sickafus, John M. Wills and Norman W. Grimes. "Structure of spinel" *J. Am. Ceram. Soc.* **82** (1999) 3279.
- [33] PHILIP W. Anderson, "Ordering and antiferromagnetism in ferrites" *Phys. Rev.* **102** (1956) 1008.
- [34] Daliya S. Mathew, and Ruey-Shin Juang, "An overview of the structure and magnetism of spinel ferrite nanoparticles and their synthesis in microemulsions" *chem. Eng. J.* **129** (2007) 51.
- [35] R. J. Armstrong, A. H. Morrish, and G. A. Sawatzky, "Mossbauer study of ferric ions in the tetrahedral and octahedral sites of a spinel" *Phys. Lett.* **23** (1966) 414.
- [36] V. G. Harris, N. C. Koon, C. M. Williams, Q. Zhang, M. Abe, J. P. Kirkland, and D. A. McKeown, "Direct measurement of octahedral and tetrahedral site environments in NiZn-ferrites" *IEEE Trans. Magn.* **31** (1995) 3473.
- [37] V. G. Harris, N. C. Koon, C. M. Williams, Q. Zhang, M. Abe, and J. P. Kirkland, "Cation distribution in NiZn-ferrite films via extended x-ray absorption fine structure" *Appl. Phys. Lett.* **68** (1996) 2082.
- [38] A. Baykal, M. S. Toprak, and H. Bayrakdar, "Synthesis and Characterization of NiFeO Nano-2 4 Octahedrons by EDTA-Assisted Hydrothermal Method" *Turk. J. Chem* **31** (2007) 659.
- [39] S. A. Oliver, V. G. Harris, H. H. Hamdeh, and J. C. Ho, "Large zinc cation occupancy of octahedral sites in mechanically activated zinc ferrite powders" *Appl. Phys. Lett.* **76** (2000) 2761.
- [40] H. Ihara, K. Tanaka, Y. Tanaka, A. Iyo, N. Terada, M. Tokumoto, M. Ariyama, I. Hase, A. Sundaresan, and N. Hamada, "Mechanism of T_c enhancement in $\text{Cu}_{1-x}\text{Tl}_x$ -1234 and-1223 system with $T_c > 130$ K" *Physica C* **341** (2000) 487.
- [41] M. Mumtaz, S. Hasnain, A. Khurram, and N. A. Khan, "Fluctuation induced conductivity in $(\text{Cu}_{0.5}\text{Tl}_{0.5-x}\text{K}_x)\text{Ba}_2\text{Ca}_3\text{Cu}_4\text{O}_{12-\delta}$ superconductor" *J. Appl. Phys.* **109** (2011) 023906.
- [42] R. Awad, "Enhancement the formation of (Cu, Tl)-1223 superconducting phase by Cd-substitution" *J. Alloys Compd.* **474** (2009) 517.

Chapter 2: Literature review

2.1. Literature review of superconducting composites

The variation in superconducting properties of $(\text{Cu}_{0.5}\text{Tl}_{0.25}\text{Pb}_{0.25})$ -1223 superconductor composites after the addition of ZnO nanoparticles were investigated [1]. Properties which show variations are critical temperature (T_c), critical current density (J_c) and phase volume fraction. It was observed that these properties showed much improvement after the addition of these nanoparticles up to a certain optimum level or (0.08 wt. %). Moreover, it was observed that at high concentration of these nanoparticles ($y > 0.8$ wt. %), the grain boundaries become more resistive and as a result increase in secondary phase was observed. On the other hand, at low concentration of these nanoparticles the resistance of these grain boundaries decreases so as outcome the increased in phase volume fraction was observed. As compared to CuTl-1223 superconductor, the presence of Pb results in decrease of critical temperature.

The $\text{GdBa}_2\text{Cu}_3\text{O}_{7.8}$ superconducting properties after the addition of ZnFe_2O_4 nanoparticles were investigated [2]. From XRD analysis data, it was observed that after the addition of ZnFe_2O_4 nanoparticles up to (0.06 wt. %) the volume fraction of Gd-123 increased. Slight retardation was also observed with further increase of zinc ferrite concentration. SEM images shows the reduction of inter-grain voids after the addition of nanoparticles up to optimum level. For determination of superconducting transition temperature electric resistivity and ac magnetic susceptibility measurements were used and it was found that when concentration of zinc ferrite increased up to (0.06 wt. %), then T_{cs} got higher and with further increased it got decreased. As compared to free sample at 77K, the magnitude of critical current density J_c increased by 1.6 orders with concentration of nanoparticles up to (0.06 wt. %). It was also observed that, after the addition of ZnFe_2O_4 nanoparticles, phase micro-hardness improved. Moreover, Hays–Kendall, Meyer's law, PSR model and elastic/plastic deformation model are the different models which were used for study of micro-hardness results

The influence of Cr_2O_3 addition on electrical transport and superconducting properties of $(\text{Bi,Pb})\text{--Sr--Ca--Cu--O}$ system were investigated in detail [3]. For samples synthesis two steps solid state reaction method was used. The Cr_2O_3 added in host material in 0, 0.3, 0.5, 0.7 and 1.0 wt. % ratios. After the addition, the maximum value of superconducting transition temperature T_c and current density J_c were observed for sample having 0.5 wt. % ratio of Cr_2O_3 . The highest (82.25%)

increased in volume fraction of 2223 phase was also observed up to optimal level. From observations, it was concluded that superconducting and transport properties of Bi-based samples were improved when Cr_2O_3 added in appropriate ratio. Also in over-doped samples with Cr_2O_3 contents, the inter-granular coupling decreased and on other hand the ratio of inter-grain weak links increased and as result these samples had minimum value of critical temperature. The critical current density J_c enhanced to 145.6 A/cm^2 for sample with 0.5 wt % of Cr_2O_3 contents. While overall decreased in J_c shows decreasing trend.

The superconducting properties of $\text{Cu}_{0.5}\text{Tl}_{0.5}\text{Ba}_2\text{Ca}_2\text{Cu}_3\text{O}_{10-\delta}$ (CuTl-1223) superconducting matrix were studied after the addition of magnetic NiFe_2O_4 nanoparticles [4]. Solid state reaction was used for the synthesis of superconducting matrix while sole-gel method was used for nanoparticles synthesis. For the characterization of the $(\text{Ni}_2\text{Fe}_2\text{O}_4)_x/\text{CuTl1223}$ composites XRD, SEM, FTIR & RT measurements were used. The XRD pattern of $(\text{NiFe}_2\text{O}_4)_x/\text{CuTl-1223}$ composites show that the superconducting matrix remains unaltered after addition of $\text{Ni}_2\text{Fe}_2\text{O}_4$ nanoparticles. The increase in normal state resistivity ($\rho_{300\text{K}}$) and decrease in $T_c(0)$ was observed with the increase in nanoparticles concentration. The change in $T_c(0)$ and ($\rho_{300\text{K}}$) was most probably due to pair-breaking and localization of these charges across the magnetic nanoparticles. After the inclusion of NiFe_2O_4 nanoparticles, the suppression in superconducting properties were observed which most probably due to the scattering and localization of mobile free carriers across nanoparticles at grain-boundaries.

The superconductive and dielectric properties of $\text{Cu}_{0.25}\text{Tl}_{0.75}\text{Ba}_2\text{Ca}_3\text{Cu}_4\text{O}_{12-\delta}$ composite after the addition of MgO nano-oxide were investigated [5]. The concentration of nanoparticles contents varied from $x = 0.0 \text{ wt. \%}$ to $x = 1.0 \text{ wt. \%}$ respectively. From XRD spectra it was clearly observed that, the structure remains unaltered after the addition of nanoparticles in host. From resistivity measurement it was observed that when the concentration of MgO nanoparticles increased from 0.0 to 0.8 wt. % then superconducting transition temperature T_c shown increased from 122 K to 136 K, while after reaching the optimal level further increased in particles concentration caused the suppression of T_c up to 117 K for $x = 1 \text{ wt. \%}$. Dielectric properties of all samples were also investigated at different values of temperatures varied from 113K to 300 K and at different frequencies in the range from 100 Hz to 4 MHz. From results of dielectrics properties, it was noted that for all values of x , the real part of dielectric constant is strongly dependent on the applied values of both the temperature and frequency respectively. Its noticed that, by decreasing

the temperature, dispersion in imaginary part of dielectric constant and loss factor were observed and shifted towards lower frequencies.

The inclusion effects of CoFe_2O_4 nanoparticles on the superconducting properties including structural and normal state resistivity of $\text{YBa}_2\text{Cu}_3\text{O}_7$ (Y-123) and $\text{Y}_3\text{Ba}_5\text{Cu}_8\text{O}_{18}$ (Y-358) superconducting phases were investigated [6]. The CoFe_2O_4 concentration varied up to 2 wt. %. A decrease in the lattice parameters a, b and c was observed with increased in CoFe_2O_4 concentration and plus decreased in the orthorhombicity of both phases revealed by XRD analysis. The lattice parameter c of Y-358 phase exhibits more variation as compared to Y-123 phase. The grain size reduced after the inclusion of nanoparticles of cobalt ferrite. It was observed that, the samples electric behavior changed from metallic to insulating with CoFe_2O_4 nanoparticles addition and this effect founded more prominent in Y-358 structure as compared to Y-123. Superconductivity highly suppressed after these CoFe_2O_4 inclusion and especially critical transition temperature of Y-358 phase. These outcomes may be attributed to the existence of higher disorder, when Co and Fe substitute the large number of Cu sites in Y-358 as compared to Y-123. In YBCO it was found that, higher degree of disordered in Cu sites decreased the critical transition temperature of system.

The role of SnO_2 addition on superconducting properties of $\text{Bi}_{1.6}\text{Pb}_{0.4}\text{Sr}_2\text{Ca}_2\text{Cu}_3\text{O}_{10+\delta}$ phase were scrutinize [7]. The variant concentration of SnO_2 nanoparticles were used to study the different superconducting properties of (Bi, Pb)-2223 phase. It was found that, for the SnO_2 nanoparticles addition up to $x = 0.4$ wt % the (T_c , J_c) and volume fraction of (Bi, Pb)-2223 phase increased. The transport current density J_c improved by 58.00% when SnO_2 concentration varied from 0.0 to 0.4 wt % of total mass and for same concentration of nanoparticles the T_c improved by 12.00%. The effective pinning effect of SnO_2 nanoparticles could be an expected reason for improvement in J_c . The superconducting parameters T_c , J_c and phase formation of (Bi, Pb)-2223 phase decreased when SnO_2 nanoparticles concentration exceed from 0.4 wt. % of total mass. The connectivity of superconducting grain reduced by the agglomeration effect caused by the high concentration of SnO_2 nanoparticles between the grains and hence critical current density deteriorated.

The $(\text{CaO}_2, \text{BaO and CuO})_y/\text{CuTl}$ -1223 superconducting composites were synthesized by the novel solid state reaction method [8]. The intergranular weak links of the host superconductor were found to be much improved with the increased of nanoparticles concentration as observed in

surface morphological study or SEM analysis. The nanoparticles inclusion not only healed up the micro-cracks but also increased the superconducting volume fraction. The frequency and temperature were the two most important factors on which dielectric properties are strongly dependent. The distinct properties like zero resistivity, dielectric properties and critical temperature of the host $\text{Cu}_{0.5}\text{Tl}_{0.5}\text{Ba}_2\text{Ca}_2\text{Cu}_3\text{O}_{10-\delta}$ superconductor exhibits opposite trend with nanoparticles inclusion.

The variation in microstructure and vortex pinning properties of Bi–Sr–Ca–Cu–O superconductor after inclusion of (NiO_2) nanoparticles has been investigated [9]. The 0.001, 0.002 and 0.005 were the various concentrations of NiO_2 nanoparticles that was introduced in host superconducting material. The critical temperature and lattice parameters almost remained unaffected after these nanoparticles inclusion. A suppression in vortex pinning force was observed for all added concentration of nanoparticles except the sample with $x=0.002$ concentration shows the clear enhancement at 90 K. The monotonic behavior of vortex pinning force could be observed up to the optimum level of concentration i.e. $x=0.002$ at temperatures above the depinning line and higher than critical temperature of Bi-2212 phase. In phase, Bi-2223 phase volume fraction reduced but pinning force remained unaffected. At the optimum level of NiO_2 nanoparticles concentration, the increased in flux pinning is the clear evidence of increased in current density and which of course because of improvement in inter-grain coupling.

The impact on mechanical properties of $(\text{Cu}_{0.5}\text{Tl}_{0.5})$ -1223 phase after SnO_2 nanoparticles addition was studied [10]. The addition of these nanoparticles up to 0.6 wt. % enhanced the volume fraction of CuTl -1223 phase and it was observed that beyond this concentration its value decreased. There were no peaks corresponds to Sn or SnO_2 compounds observed in XRD spectra. The Sn existence in bulk was confirmed during EDS analysis and is the clear evidence that SnO_2 nanoparticles not enter in phase original structure. The SEM results confirmed that the density of pores decreased and microstructure density increased with SnO_2 nanoparticles inclusion. By increasing the applied load up to 1.96 N, a decreasing trend in the micro-hardness of the studied samples was observed and beyond this value, its shown slight decreased. While on other hand its shown gradual increased in $(\text{Cu}_{0.5}\text{Tl}_{0.5})$ -1223 phase with SnO_2 nanoparticles addition. Therefore, it can be concluded that this addition effectively increased the phase micro-hardness.

The solid state synthesis route was used for synthesized the $\text{Bi}_{1.6}\text{Pb}_{0.4}\text{Sr}_{1.9}\text{Ca}_{2.1}\text{Cu}_3\text{O}_{10-\delta}$ superconducting matrix [11]. The added Al_2O_3 nanoparticles have the average size of 50 nm and

their concentration varied from (0.0 to 1.0 wt. %). At 77 K temperature and (0.2 wt. %) of Al_2O_3 nanoparticles concentration the 30% increase in " J_c " was found and this improved " J_c " behavior in existence of applied magnetic field either could be parallel or perpendicular surface of the sample. However, complete pbase formation could not be achieved as the Al_2O_3 nanoparticles were added in higher concentration which caused the decrease in " J_c ". So it has concluded from observation that, during the final processing of BPSCCO samples the Al_2O_3 nanoparticles addition up to optimal level effectively enhanced its flux pinning capability and also shown some disadvantages during (Bi,Pb)-2223 formation procedure.

The variation in J_c of $(\text{Bi}_{1.6}\text{Pb}_{0.4})\text{Sr}_2\text{Ca}_2\text{Cu}_3\text{O}_{10}$ superconductor after the addition of NiFe_2O_4 nanoparticles were investigated [12]. It was found that transport critical current density of all the samples after the addition of NiFe_2O_4 nanoparticles enhanced. It was observed that, the samples with (0.01 wt. %) concentration of nickel ferrite nanoparticles exhibited maximum flux pinning properties. Therefore, it was concluded from these result that, the addition of ferromagnetic nanoparticles effectively increased the critical current density J_c of the Bi-2223 superconductor. The electric transport properties can be improved if method of preparation further optimized. It was suggested that, enhancement in J_c of the host $(\text{Bi}_{1.6}\text{Pb}_{0.4})\text{Sr}_2\text{Ca}_2\text{Cu}_3\text{O}_{10}$ superconductor was due to the full vortex magnetic energy after the addition of NiFe_2O_4 nanoparticles.

The melt-texturing synthesis route was used for zirconate and calcium nanoparticles added BSCCO superconducting samples [13]. The addition of these nanoparticles effectively improved the various superconducting characteristics of Bi-2212 melt-textured composites. The critical current density J_c shows 40% increased for 1 wt. % calcium silicate nanoparticles addition. This enhancement was found to be due to the improved connectivity between grains besides the new pinning centers creation with calcium silicate addition. While in case of zirconate addition showed only the creation of flux pinning centers.

The variation in $\text{YBa}_2\text{Cu}_3\text{O}_{7-\delta}$ (YBCO) superconducting and transport properties after Fe_3O_4 inclusion were studied [14]. The Fe_3O_4 nanoparticles have average size of 28 nm and their concentration in $\text{YBa}_2\text{Cu}_3\text{O}_{7-\delta}$ superconductor varied from (0.01- 0.05 wt. %). The Four-probe method used to find out T_c . It was found that sample with 0.002 wt. % concentration exhibited the highest T_c at 87 K temperature. Also at 77 K temperature the same sample had highest J_c value up to 1683 mA/cm^2 . It's indicated that in YBCO superconductor the Fe_3O_4 nanoparticles acts as

effective source of flux pinning centers. It was observed up to optimal value of Fe_3O_4 nanoparticles addition T_c and J_c of the sample increased while its excessive addition over all suppressed the superconducting characteristics. The thermally activated flux creep plays a major role in suppression of J_c with increased in temperature. The magnetic impurities also the cause of suppressing the superconductivity of the samples. Therefore, it was proposed that, overall the magnetic nanoparticles inclusion improved the J_c of YBCO superconductor.

In absence of applied field, superconducting transport properties of $(\text{ZnFe}_2\text{O}_4)_y/\text{CuTl-1223}$ superconductor composites were investigated [15]. Solid state reaction and sol gel methods were used for synthesis of superconducting matrix and ZnFe_2O_4 nanoparticles respectively. XRD, SEM, FTIR and RT measurements were used to characterize the composites. Both FTIR and XRD results showed no change in tetragonal structure of CuTl-1223 composites after the addition of ZnFe_2O_4 nanoparticles. SEM images showed that the inclusion of ZnFe_2O_4 nanoparticles results in improvement of grain size. Magnitude of diamagnetism and $T_c(0)$ decreased with the addition of ZnFe_2O_4 nanoparticles. The most possible reason of decrease in superconducting properties with the induction of ZnFe_2O_4 nanoparticles in host $(\text{Cu}_{0.5}\text{Tl}_{0.5})\text{-1223}$ superconductor matrix was the reflection of spin charge due to paramagnetic nature of zinc ferrite nanoparticles and the confinement of inobile free carriers. Incorporation of Zn and Fe in lattice sites may cause decrease of composites critical temperature $T_c(0)$. The superconducting properties of these composites exhibited non-monotonic alteration which was probably due to not uniform distribution of zinc ferrite nanoparticles at inter grain boundaries of CuTl-1223 superconductor.

The various concentration of Co_3O_4 nanoparticles were added to (Bi, Pb)-2223 system and as a results alteration in superconducting properties were studied [16]. The samples in which the concentration of Co_3O_4 nanoparticles is 0.01 wt. % had higher T_c value of 102 K as compared to the pure sample which exhibited the T_c up to 100 K. The highest fraction of 2223 phase was observed in sample. It was observed that, the flow of supercurrents obstructed due to increase in Co contents. The results show that, the T_c strongly dependent on size of Co_3O_4 nanoparticles. Even though the samples superconductivity overall suppressed with addition of magnetic impurities but with appropriate addition of these nanoparticles increased the various superconducting properties of Bi-based samples. While, with excessive Co_3O_4 nanoparticles inclusion caused the degradation in superconductivity of Bi-2223 phase.

The superconducting properties of $\text{FeSe}_{0.5}\text{Te}_{0.5}$ showed significant enhancement after the addition Sn nanoparticles [17]. These improvements in superconducting properties include enhancement in T_c^{onset} (K) and sharpness of transition width. The measured value of J_c was $7 \times 10^3 \text{ A cm}^{-2}$ for the sample with Sn addition. While at 4.3 K, the same sample maintained or carry a stable value of J_c up to $3 \times 10^2 \text{ A cm}^{-2}$ even beyond 60,000 Oe as compared to Sn nanoparticles free samples. The morphological and phase compositional characterizations both conformed that, the Sn addition affectively facilitate the superconducting phase formation while suppresses the Fe_7Se_8 impurity and amorphous phase formation. So consequently, J_c improved.

References

- [1] M. M. Elokr, R. Awad, Asmaa Abd El-Ghany, A. Abou Shama, and A. Abd El-wanis, "Effect of Nano-Sized ZnO on the Physical Properties of $(\text{Cu}_{0.5}\text{Tl}_{0.25}\text{Pb}_{0.25})\text{Ba}_2\text{Ca}_2\text{Cu}_3\text{O}_{10-\delta}$ " *J. Supercond. Novel Magn.* **24** (2011) 1345.
- [2] R. Awad, Al Abou Aly, N. H. Mohammed, S. Isber, H. A. Motaweh, and D. El-Said Bakeer, "Investigation on superconducting properties of $\text{GdBa}_2\text{Cu}_3\text{O}_{7-\delta}$ added with nanosized ZnFe_2O_4 " *J. Alloys Compd.* **610** (2014) 614.
- [3] H. Abbasi, J. Taghipour, and H. Sedghi, "Superconducting and transport properties of $(\text{Bi-Pb})\text{-Sr-Ca-Cu-O}$ with Cr_2O_3 additions" *J. Alloys Compd.* **494** (2010) 305.
- [4] K. Nadeem, G. Hussain, M. Mumtaz, A. Haider, and S. Ahmed, "Role of magnetic NiFe_2O_4 nanoparticles in CuTl-1223 superconductor" *Ceram. Int.* **41** (2015) 15041.
- [5] N. H. Mohammed, "Effect of MgO Nano-oxide Additions on the Superconductivity and Dielectric Properties of $\text{Cu}_{0.25}\text{Tl}_{0.75}\text{Ba}_2\text{Ca}_3\text{Cu}_4\text{O}_{12-\delta}$ Superconducting Phase" *J. Supercond. Novel Magn.* **25** (2012) 45.
- [6] Y. Slimani, E. Hannachi, MK Ben Salem, A. Hamrita, A. Varilci, W. Dachraoui, M. Ben Salem, and F. Ben Azzouz, "Comparative study of nano-sized particles CoFe_2O_4 effects on superconducting properties of Y-123 and Y-358" *Physica B* **450** (2014) 7.
- [7] A. I. Ahou-Aly, MMH Abdel Gawad, R. Awad, and I. G-Eldeen, "Improving the physical properties of $(\text{Bi, Pb})\text{-2223}$ Phase by SnO_2 Nano-particles addition" *J. Supercond. Novel Magn.* **24** (2011) 2077.
- [8] M. Mumtaz, M. Kamran, K. Nadeem, Ahdul Jabbar, Nawazish A. Khan, Abida Saleem, and S. Tajammul Hussain, "Dielectric properties of $(\text{CuO, CaO}_2, \text{ and BaO})_y/\text{CuTl-1223}$ composites" *J. Low Temp. Phys.* **39** (2013) 622.
- [9] B. A. Alhiss, I. M. Obaidat, M. Gharaibeh, H. Ghamlouche, and S. M. Obeidat, "Impact of addition of magnetic nanoparticles on vortex pinning and microstructure properties of Bi-Sr-Ca-Cu-O superconductor" *Solid State Comm.* **150** (2010) 1542.

- [10] N. H. Mohammed, A. I. Abou-Aly, I. H. Ibrahim, R. Awad, and M. Rekaby, "Mechanical properties of $(\text{Cu}_{0.5}\text{Tl}_{0.5})\text{-1223}$ added by nano- SnO_2 " *J. Alloys Compd.* **486** (2009) 733.
- [11] M. Annabi, A. Mchirgui, F. Ben Azzouz, M. Zouaoui, and M. Ben Salem, "Addition of nanometer Al_2O_3 during the final processing of $(\text{Bi}, \text{Pb})\text{-2223}$ superconductors" *Physica C* **405** (2004) 25.
- [12] W. Kong, R. Abd-Shukor, "Enhanced electrical transport properties of nano NiFe_2O_4 -added $(\text{Bi}_{1.6}\text{Pb}_{0.4})\text{Sr}_2\text{Ca}_2\text{Cu}_3\text{O}_{10}$ superconductor" *J. Supercond. Novel Magn.* **23** (2010) 257.
- [13] Dayse I. dos Santos, Jung Ho Kim, M. Qin, Konstantin Konstantinov, and S. X. Dou, "Addition of Ca-compounds nanoparticles in melt-textured Bi: 2212" *Physica C* **460** (2007) 1329.
- [14] Abd-Ghani, Siti Nurdalila, Roslan Abd-Shukor, and Wei Kong, "Effects of Fe_3O_4 Nano Particles Addition in High Temperature Superconductor $\text{YBa}_2\text{Cu}_3\text{O}_{7-\delta}$ " *Adv. Mater. Res.* **501** (2012) 309.
- [15] M. Mumtaz, S. Naeem, K. Nadeem, F. Naeem, Abdul Jabbar, Y. R. Zheng, Nawazish A. Khan, and M. Imran, "Study of nano-sized $(\text{ZnFe}_2\text{O}_4)_y$ particles/ CuTl-1223 superconductor composites" *Solid State Sci.* **22** (2013) 21.
- [16] A. N. Jannah, R. Abd-Shukor, and H. Abdullah, "Effect of Co_3O_4 Nanoparticles Addition on $(\text{Bi}, \text{Pb})\text{-2223}$ Superconductor" *Int. J. Math. Comput. Phys.* **7** (2013) 362.
- [17] Chen, Ning, Yongchang Liu, Zongqing Ma, and Huijun Li, "Significant enhancement of superconducting properties in the $\text{FeSe}_{0.5}\text{Te}_{0.5}$ bulks by minor Sn addition" *Mater. Lett.* **175** (2016) 16.

Chapter 3: Synthesis and Characterization Techniques

3.1 Synthesis of nanoparticles

The two most popular approaches to synthesize the nanoparticles are physical (top down) approach and second is chemical (bottom up) approach. The synthesis of nanoparticles through physical method involve reduction of bulk size material or simply its subdivision to obtain nanoparticles in large amount. While on other hand, chemical method for particles synthesis by nucleation of atoms, ions and molecules is one of the best way to synthesize the required particles. In this method, we can control both size and chemical composition of particles to reproduce them with same results [1]. The Fig 3.1 is the schematic representation of both approaches.

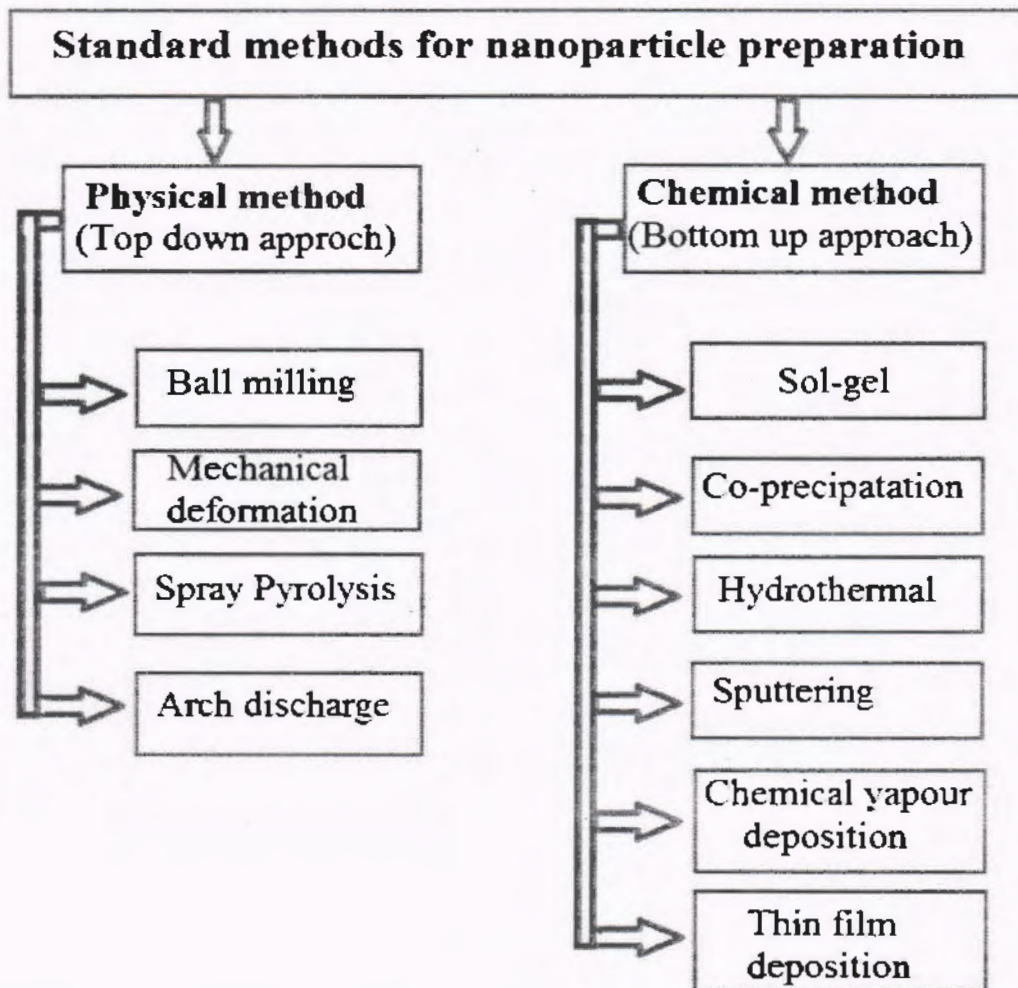


Fig 3.1: List of different physical and chemical methods for particle synthesis.

3.1.1 MnFe₂O₄ nanoparticles synthesis

For synthesis of manganese ferrite (MnFe₂O₄) nanoparticles, we used Sol-gel method. During first step, the two different solutions are prepared. One solution contain iron nitrate and manganese nitrate mixed with ethanol and second solution prepared by mixing citric acid with distilled water. Then stirred the mixture of both these solutions and more precisely adjusted its pH value up to 5 with the help of ammonia addition drop by drop. The entire process for manganese ferrite nanoparticles synthesis schematically demonstrated in Fig. 3.2.

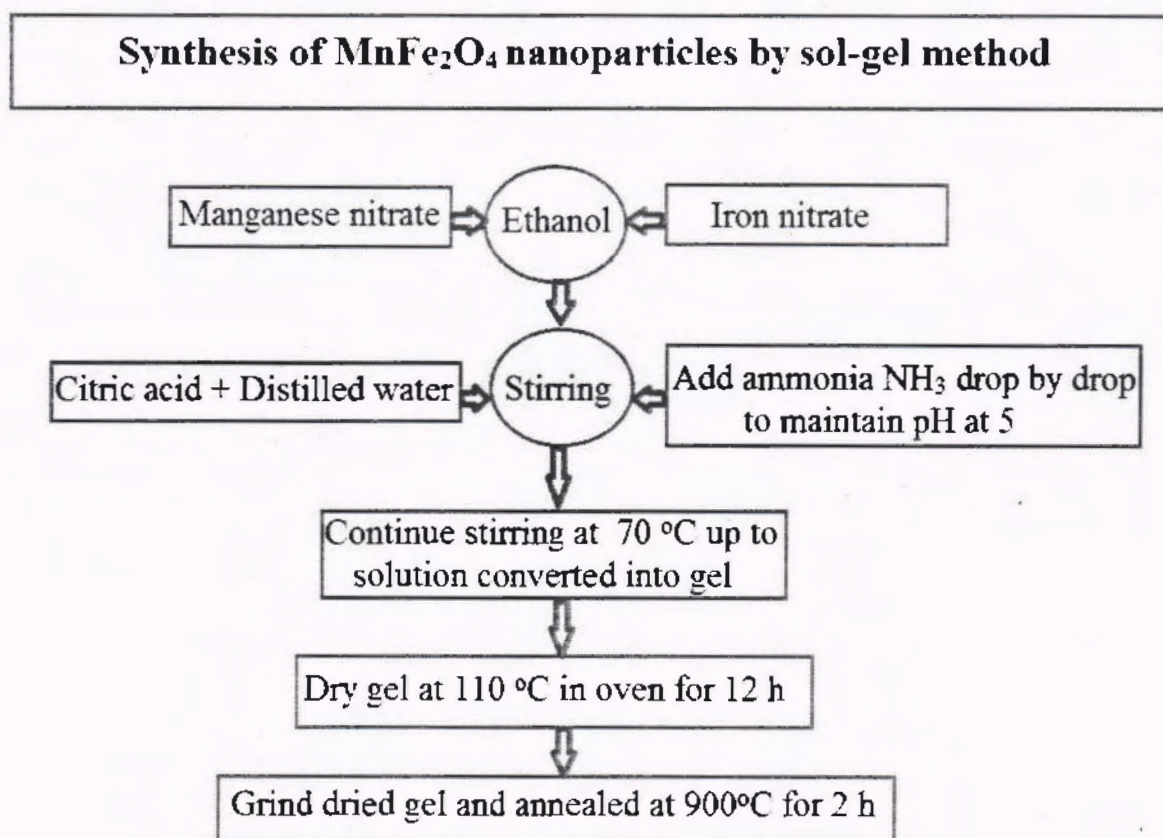


Fig 3.2: Complete flow chart of MnFe₂O₄ nanoparticles.

It was observed, after adjusting the pH value up to 5 and then heating at 70°C temperature with continuous stirring converted the whole solution into gel like form in round about 15 minutes approximately. Now at this stage we stopped the stirring process and placed the gel like solution into oven for 12 hours at a temperature of 110°C. Then grind the resultant dry gel to obtain fine

powder after annealed it 900°C exactly about 2 hours in chamber furnace. After completing this entire process of grinding and annealing, manganese ferrite nanoparticles are the resultant product.

3.1.2 $\text{Cu}_{0.5}\text{Tl}_x\text{Ba}_2\text{Ca}_2\text{Cu}_3\text{O}_{10-\delta}$ precursor synthesis

To synthesized the CuTI-1223 ($\text{Cu}_{1-x}\text{Tl}_x\text{Ba}_2\text{Ca}_2\text{Cu}_3\text{O}_{10-\delta}$) through solid state reaction we initially used three compounds $\text{Ca}(\text{NO}_3)_2$, $\text{Ba}(\text{NO}_3)_2$ and $\text{Cu}_2(\text{CN})_2 \cdot \text{H}_2\text{O}$ in proper ratios. After mixing the above mention compounds in appropriate ratios next step was to grind the mixture in agate mortar and pestle for 4 hours approximately. Then we loaded the mixture in quartz boat to placed it inside the chamber furnace about 24 hours at a high temperature of 860°C. After exactly 24 hours, furnace is switch off and mixture was furnace cooled. The heat treatment process at 860°C temperature is repeated after grinding the mixture for one hour to get the resultant precursor. To understand $\text{Cu}_{0.5}\text{Tl}_x\text{Ba}_2\text{Ca}_2\text{Cu}_3\text{O}_{10-\delta}$ synthesis process the schematic chart is as shown in Fig. 3.3.

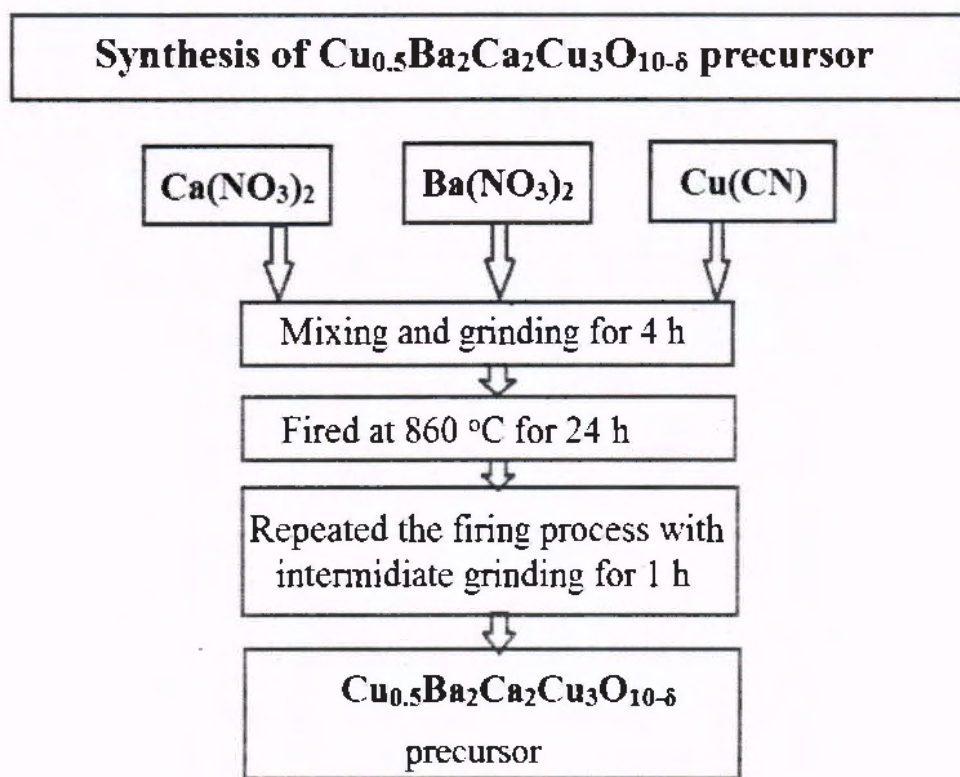


Fig 3.3: Various steps involved in $\text{Cu}_{0.5}\text{Ba}_2\text{Ca}_2\text{Cu}_3\text{O}_{10-\delta}$ precursor synthesis.

3.1.3 Synthesis of $(\text{MnFe}_2\text{O}_4)_x/\text{CuTl-1223}$ nanoparticles composites

We individually synthesized both the $(\text{MnFe}_2\text{O}_4)$ nanoparticles and $(\text{Cu}_{0.5}\text{Tl}_x\text{Ba}_2\text{Ca}_2\text{Cu}_3\text{O}_{10-\delta})$ precursor. We mixed various concentration of manganese ferrite nanoparticles ($x=0, 0.5, 1, 1.5$ and 2 wt. %) plus thallium oxide Tl_2O_3 in precursor material. Then grind the mixture for duration of one to two hours and then pelletized each of these samples with help of hydraulic press. All the pellets were warped in the gold capsule and sintered at a constant temperature of 860°C for 10 minutes. This entire process of $(\text{MnFe}_2\text{O}_4)_x/\text{CuTl-1223}$ nanoparticles superconductor composites is as shown below in Fig. 3.4.

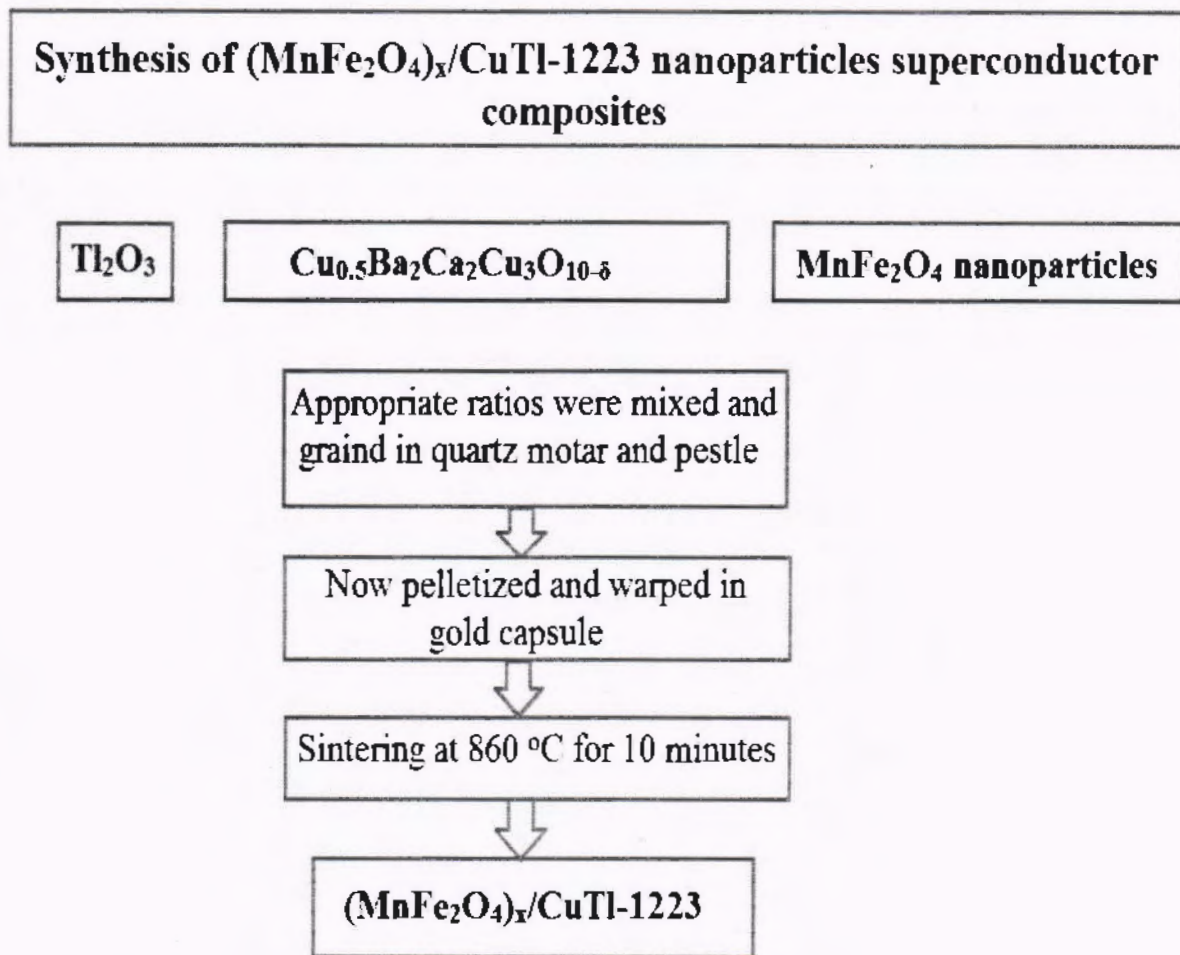


Fig 3.4: Flow chart of $(\text{MnFe}_2\text{O}_4)_x/\text{CuTl-1223}$ nanoparticles superconductor composite.

3.2 Experimental characterization techniques

The following techniques were used to characterize the resultant composites;

1. X-ray diffraction (XRD)
2. Scanning electron microscope (SEM)
3. R-T measurements

3.2.1 X-rays diffraction (XRD)

The materials classification is based on the atoms arrangement in the crystal. In periodic arrangement the atoms arranged their self in large numbers of series and form the parallel planes to each other. These planes have specific distance between them and by calculating this distance, we can find the various parameters of a unit cell, structure of the unit cell, crystal defects, concentration of impurities in crystal etc., [2].

The very shorter wavelength of the X-rays allows them to penetrate deep into the materials and also having property to diffraction from the atoms of these materials. The target material which is normally used for X-ray generation is copper and the resultant X-rays which are produced have wavelength about 1.54 Å [3]. The basic principle of X-ray diffraction based on the interaction of X-ray of wave length λ with material and the detection of diffracted X-rays from the material by the detector [4]. Bragg's Law is used for the explanation of diffraction pattern.

3.2.1.1 Basic principle

The X-ray beam when incident on the crystal interact with its atoms then it accelerates the electron oscillations as shown in Fig. 3.6. Frequency of both incident beam and oscillating electrons mostly identical. The distractive interference will be observed as result of out of phase ray's interaction and contrary to this constructive interference take place in the direction of regular and periodic arrangement of atoms and cause by in phase rays interactions. The Bragg's Law well explained this phenomena of constructive interference [5]. The XRD basic working mechanism is schematically as shown in Fig. 3.5.

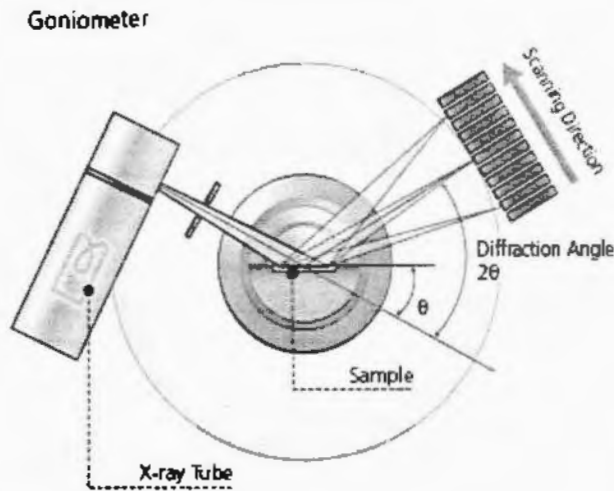


Fig 3.5: Working principle of XRD apparatus.

3.2.1.2 Bragg’s Law

The famous Bragg’s Law was derived in 1912 by W. L. Bragg and W. H. Bragg. For the X-rays where the wavelength of these rays is smaller than the lattice constant under such condition the diffraction of X-rays take place and it is clearly observed that direction of diffracted X-rays is opposite to incident rays. So there for the diffraction of X-rays take place only when the Bragg condition is satisfied for constructive interference.

We consider a case of parallel planes where the inter-planner distance can be represented by d. observation shows that, the measured path difference between the two consecutive reflected X-rays was found to be $2d\sin\theta$. Where θ can be measured from the given diagram. The constructive interference take place under the condition where the path difference is found to be an integral number m of the wavelength λ of X-rays, therefore in equation form, it can be written as [6].

$$m\lambda = 2d\sin\theta \dots\dots\dots 3.1$$

Above equation is also known as Bragg’s Law. This equation must be satisfied in case where $\lambda \leq 2d$.

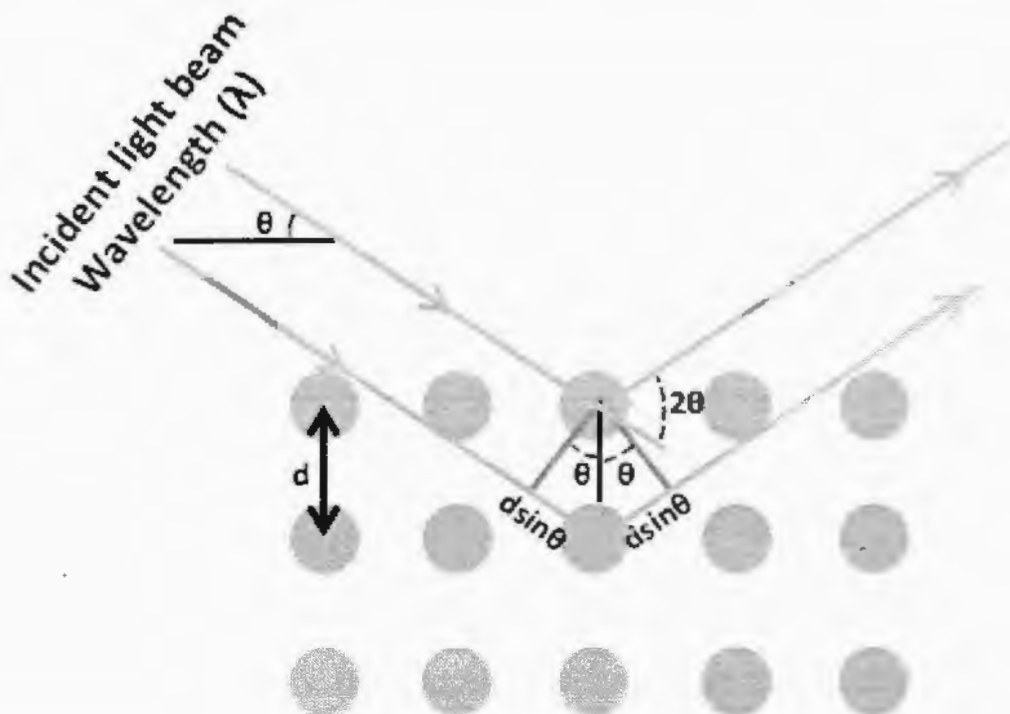


Fig 3.6: Bragg's Law schematic illustration of X-rays diffraction from crystal planes.

3.2.1.3 Powder diffraction method

In this diffraction method, powder form of sample is exposed to the beam of X-rays. The value of wavelength λ remains unaltered while prominent change in the value of angle θ varied constantly. For the characterization of superconductors, mostly the powder diffraction method is used. This method is very accurately calculated the various parameters including inter planner distance or d spacing, diffraction angles and other different cell parameters.

3.2.1.4 Different parts of X-rays diffractometer

X-rays diffractometer consist of following parts explained below;

1. Source of X-rays:

In this part different metal are used for the production of X-rays..

2. Goniometer:

This component basic purpose is to control the rotation of sample holder.

3. Electronic Circuit Panel (ECP):

All process of X-rays count and detection accomplished by ECP electronically [7].

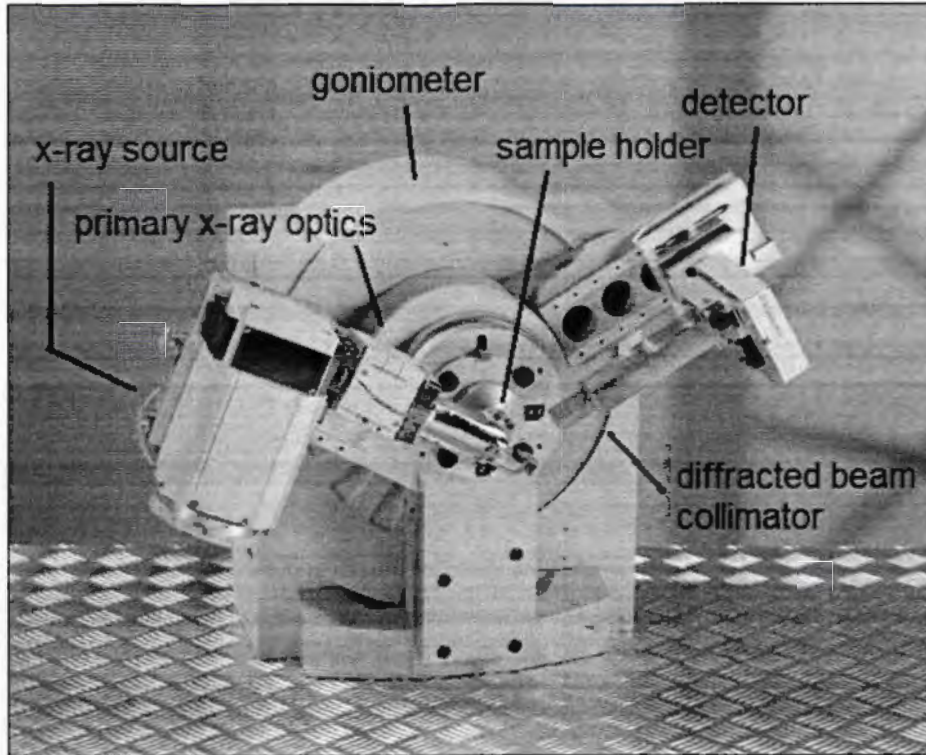


Fig 3.7: X-ray diffractometer with various labeled parts.

3.2.1.5 Major application of XRD

In field of material science, XRD is an important tool of characterization. The most well know applications are

1. Determination of atoms arrangement.
2. Measuring the spacing or d spacing.
3. Different crystalline phase's determination.
4. Used for finding the integrated intensities.
5. Identification of unknown crystal structure.

3.2.2 Scanning electron microscope (SEM)

This is one of the most advance version of electron microscope. It is used to scan the surface of the materials and formed images to study the different features at the surface of material. The conventional light microscope work based on beam of photon while the beam of electron used in all electron microscopes. The resolution capability of SEM is comparatively very higher than any other microscopes. The unique feature of SEM is its EDS or EDX part. This part use X-rays to find out the elemental composition of the material [8-10]. The SEM diagram with labeled parts is as shown in Fig.3.8.



Fig 3.8: Scanning electron microscope (SEM).

3.2.2.1 Different parts of SEM

The Electron Gun

The electron gun is positioned at very top or bottom of the column and its purpose is to produce very intense electron beam. Conventionally two types of electron guns that are normally used are

Thermionic Gun

In this type of gun, the material used for filament fabrication is normally tungsten and it is used because of its high melting point. When thermal energy is supplied to the filament, electrons are emitted from the filament in the form of an electron beam that later fall upon the specimen.

Field Emission Gun

In this type of electron gun, the electrons are ejected from atoms by applying a strong electric field. As compared to a thermionic gun, this electron gun has more advanced features.

Lenses

The lenses used in SEM have the same function just like the lenses used in an ordinary optical microscope. However, the images formed by SEM lenses are more magnified and clear for detail studies. The lenses used in SEM are made up of magnets that are also known by the name of condenser lenses. The unique capability of these condenser lenses is to de-magnify the electron beam for the purpose of focusing it on the target specimen. The objective lens is another condenser lens used for the purpose of controlling the electron beam size that later strikes the surface of the target sample.

Scanning System

In this part, the beam of electrons scans the target sample in a regular manner to form its image for further study purposes. The electron beam can be pushed or deflected with the help of a scanning coil.

Sample Chamber

In this chamber, we place our test subject or sample that needs to be examined. The extremely static position during the scanning process is compulsory to get a clear image. So therefore the sample

chamber must be isolated from externally or internally created vibrations. Sample chamber can change the samples angle at which it placed for scanning process.

Detector

The detectors in SEM plays a very vital role to detect various signals. When the beam of electron strikes the target sample, various electrons are produces each carry the different information and various detectors in SEM detect these electrons. In SEM the role of Everhart-Thorny detector is to detect the secondary electrons that are very useful to produced detail images. While the function of X-ray detector and BSE detector to find out the various elemental compositions.

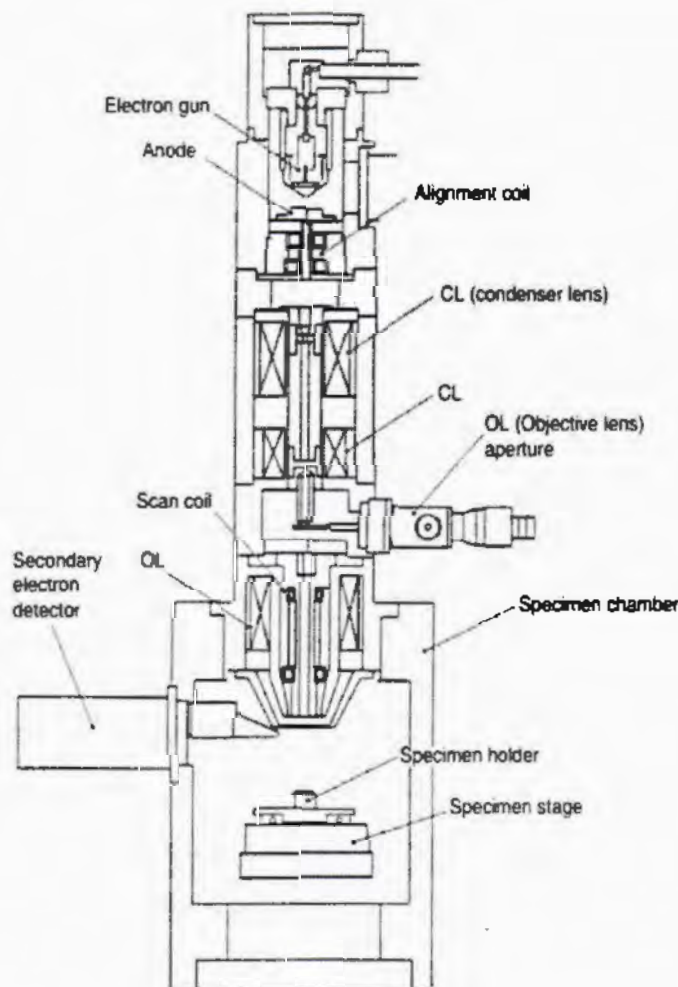


Fig 3.9: Schematic diagram of SEM various parts [11].

3.2.2.2 Energy dispersive X-rays analysis (EDX)

This technique widely used to identify the elemental composition of any compound very accurately and commonly known by the name of (EDX) analysis [12]. The EDX is an integrated feature of SEM apparatus. The basic principle of EDX analysis based on emission of characteristic x-rays from a target sample or specimen when incident x-rays beam strikes it. This incident X-ray beam consist of huge number of high-energy electrons. As we know that, usually the electron inside an atom always occupy discrete energy levels. So therefore, when incident x-ray beams excite electrons from any lower shell by creating a vacancy, which filed by the electrons from some higher energy shell by releasing its excess energy in form the X-rays.

3.2.3 Four-probe method used for resistivity measurements

For resistivity measurements of any superconductor, mostly the four-probe method is used. Through this method, we not only measure the resistivity but also can find its critical temperature $T_c(R=0)$ of our specific material. The few very conventional reasons for resistivity of any conducting material are atomic scale vibrations or simply atomic vibrations, irregular electron-electron interaction produced by the presence of defects in crystal lattices [13-14].

For the practical use of four-probe, we attached all four probe to the surface of the rectangular bar shape sample through low resistance contacts. Ohms law is very useful in resistivity measurements

$$R = \frac{V}{I} \dots\dots\dots 3.2$$

In above equation V and I represent the applied voltage and current respectively. It was also found that the resistance is strongly depend on the geometry of given sample i.e.

$$R \propto \frac{L}{A} \dots\dots\dots 3.3$$

Therefore, the resistance R is clearly directly proportional to length L and inversely proportional to A area of the sample.

$$R = \rho \frac{L}{A} \dots\dots\dots 3.4$$

Where ρ used to designate the resistivity and it is intrinsic characteristic of the material.

$$\rho = \frac{RA}{L} \dots\dots\dots 3.5$$

By putting the value of R from above equation

$$\rho = \frac{VA}{II} \dots\dots\dots 3.6$$

All probes connected to the sample surface in such a way that outer two probes pass the current only while middle pair of probes measure the resultant potential difference between the two points. During our process of measurements, we use a very small current about 1 or 2 mA. While liquid nitrogen is, use for measuring the temperature dependent resistivity of the sample and acts like a cryostat. In entire process of resistivity measurement, the temperature varied from 77 K to normal room temperature by applying heat in range of 1 K/min to 3 K/min [15]. The schematic diagram of four-probe method is as shown in Fig.3.10.

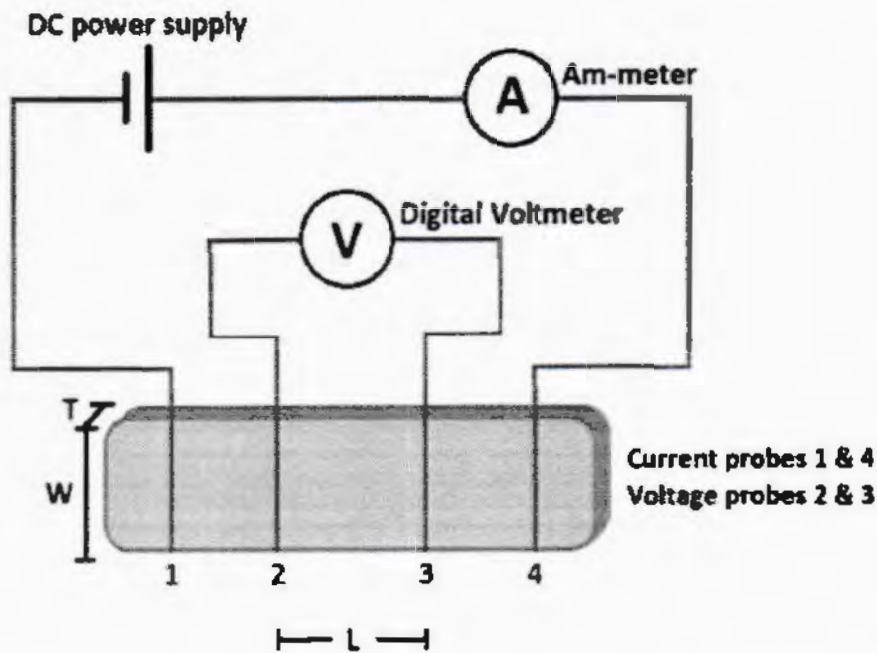


Fig 3.10: Schematic four-point probe apparatus working mechanism.

3.2.4 Fourier transform infrared FTIR spectroscopy

The FTIR is the abbreviation conventionally used to represent the Fourier transform infrared spectroscopy. This spectroscopy technique involves the interactions among matter and EM field in the infrared region. When IR radiations incident upon the sample than some part of these incident radiations absorbed and rest transmitted through the specimen or sample. The molecules acquired the higher vibrational energy state after absorbing these radiations. In other words, IR absorption takes place only if the alteration in molecular dipole occurs because of interaction between matter and IR radiations. The resultant spectrum exhibits the molecular absorption, transmission and include molecular fingerprints of specimen. So the composition of each element is different so it is not possible that two elements showing identical Infrared spectrum [16-17]. FTIR spectrometer is the main part of FTIR apparatus. The Michelson interferometer utilized inside the spectrometer and its basic principle demonstrated below in Fig. 3.11.

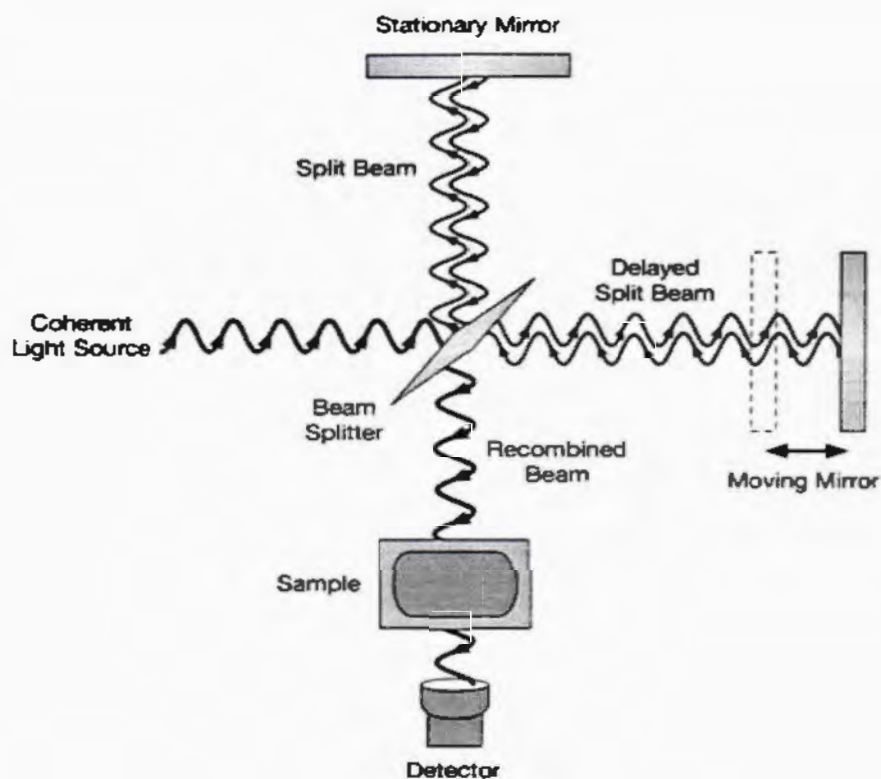


Fig 3.11: Working principle of FTIR and its various parts.

For characterization, small quantity of our sample is mixed with KBr for pelleting purpose. FTIR spectrometer collects the background spectrum of KBr and then sample spectrum. The spectrometer is very efficiently subtracted the background spectrum and gives us the sample spectrum only. The practical FTIR apparatus image is as shown in Fig 3.12.



Fig 3.12: Modern FTIR apparatus at present time.

References

- [1] Cao, Guozhong, "Synthesis properties and applications" Imperial college press, London, (2004).
- [2] B. E. Warren, X-ray Diffraction. Dover Publications, (1969).
- [3] H. P. Klug, and L. E. Alexander, "X-Ray diffraction procedures for polycrystalline and Amorphous materials" Wiley, (1974).
- [4] G. Gilli, "Fundamentals of Crystallography" Oxford university press, U.K. (2002).
- [5] B.E. Warren, "X-ray Diffraction" Courier corporation, U.S.A. (1969).
- [6] C. Kittel, "Introduction to solid state physics" 7th ed. Wiley, India (1995)
- [7] H. P. Klug, and L. E. Alexander, "X-Ray diffraction procedures: for polycrystalline and amorphous materials" 2nd ed. Wiley-interscience, New York (1974).
- [8] B.Cheney, "Introduction to scanning electron microscopy" San Jose State University press (1995).
- [9] L. Reimer, Scanning electron microscopy, "Physics of image formation and microanalysis" Springer, (1998).
- [10] J. Cazaux, "Mechanisms of charging in electron spectroscopy" J. Elec. Spect. Rel. Phen. **105** (1999) 155.
- [11] Tursunov, Obid, Jan Dobrowolski, Kazimierz Klima, Bogusława Kordon, Janusz Ryczkowski, Grzegorz Tylko, and Grzegorz Czerski, "The Influence of Laser Biotechnology on Energetic Value and Chemical Parameters of Rose Multiflora Biomass and Role of Catalysts for bio-energy production from Biomass: Case Study in Krakow-Poland." World J. Environ. Eng. **3** (2015) 58.
- [12] N.Unakar, J. Tsui, and C. Harding, "Scanning electron microscopy". Ophthalmic research press, U.S.A. (1981).
- [13] F. Gomory, "Characterization of high-temperature superconductors by AC susceptibility measurements" Supercond. Sci. Technol. **10** (1997) 8.
- [14] F. Gomory, "Superconductor science and technology" **10** (1997) 523.

[15] T. G. M. Kleinpenning, "Theory of noise investigations on conductors with the four-probe method," *J. Appl. Phys.* **48** (1977) 2946.

[16] P. R. Griffiths, and J. A. D. Haseth, "Fourier transform infrared spectrometry" J. Wiley & Sons, (2007).

[17] J. R. Ferraro, and L. J. Basile, "Fourier transform infrared spectroscopy: applications to chemical systems" Academic Press, (1982).

Chapter 4: Results and Discussion

4.1 X-Ray diffraction analysis

The XRD technique is most widely used for structure analysis of all materials [1]. Moreover, this technique also being used for calculating the average crystallite size of the given sample. XRD spectrum of manganese ferrite (MnFe_2O_4) nanoparticles is shown in Fig. 4.1. The peaks at $2\theta = 29.70^\circ$, 34.98° , 42.52° , 56.19° , 61.65° were indexed to (220), (311), (400), (511) and (440) which confirms spinel structures of manganese ferrite nanoparticles by following the space group Fd-3m with lattice parameter $a = 4.89 \text{ \AA}$. To estimate and find out the crystallite size of nanoparticle particles, we used Debye-Scherrer's formula

$$D = \frac{k\lambda}{\beta \cos\theta} \dots\dots\dots 4.1$$

In above equation (4.1), the D , θ , λ and K are corresponding to average crystallite size, Bragg's angle, incident rays' wavelength and a dimension less constant quantity with value of 0.9. The calculated average particle size of MnFe_2O_4 nanoparticles is '20' nm.

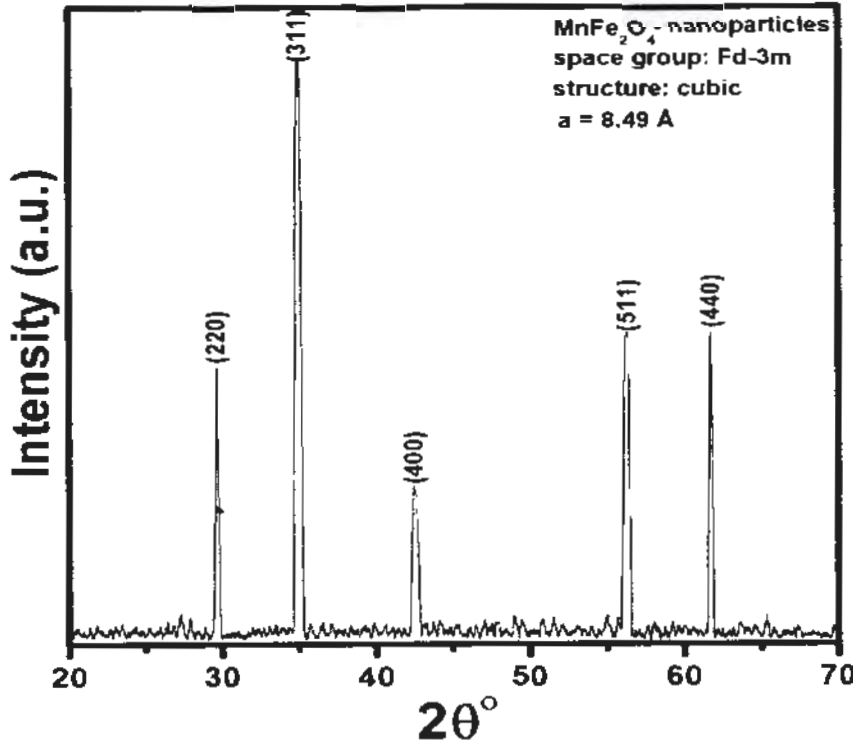
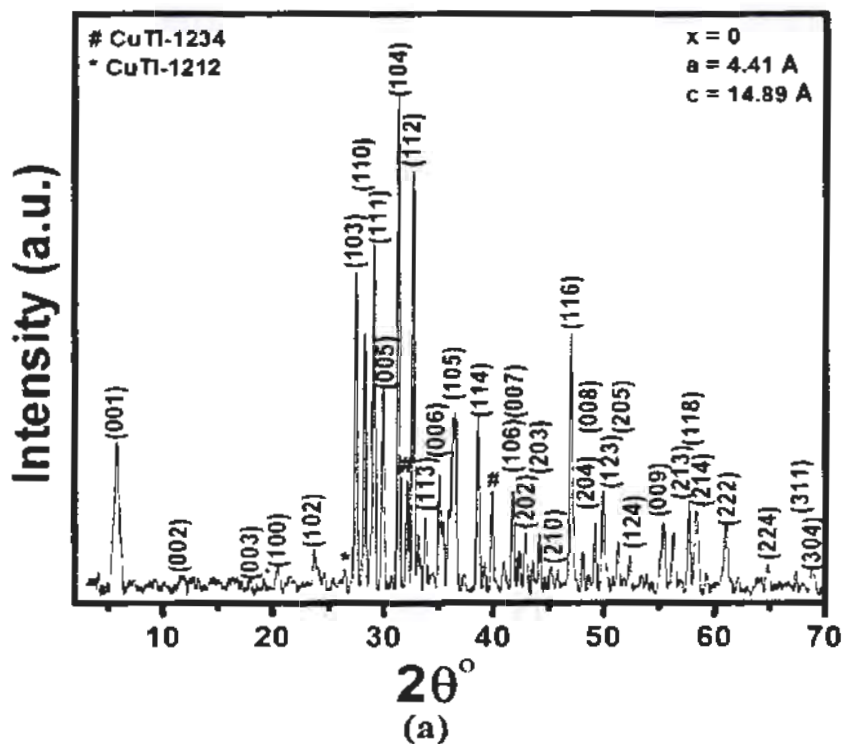
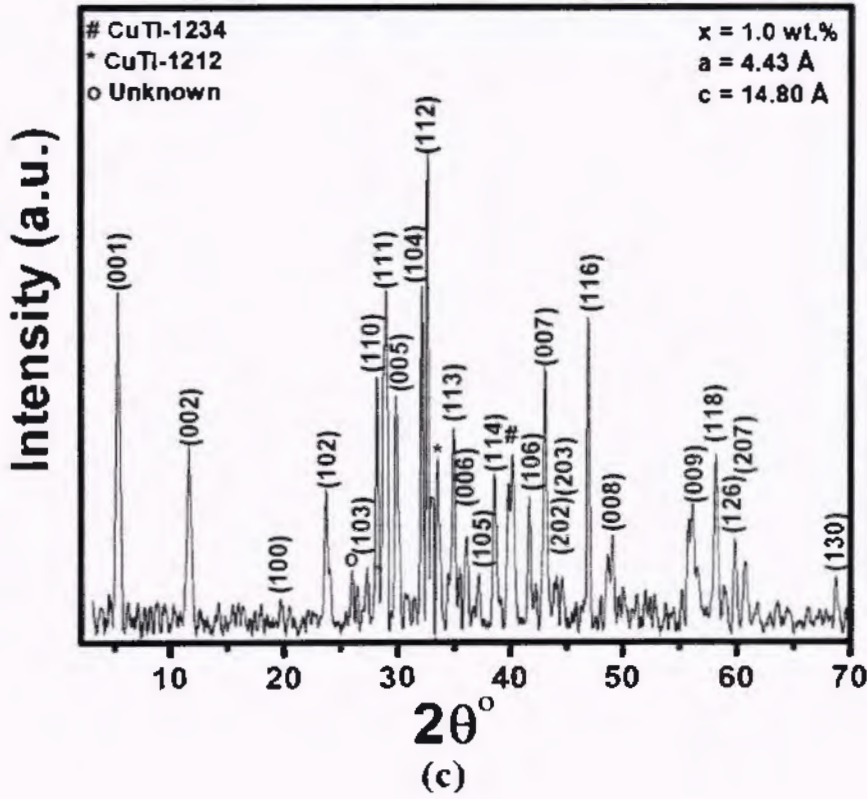
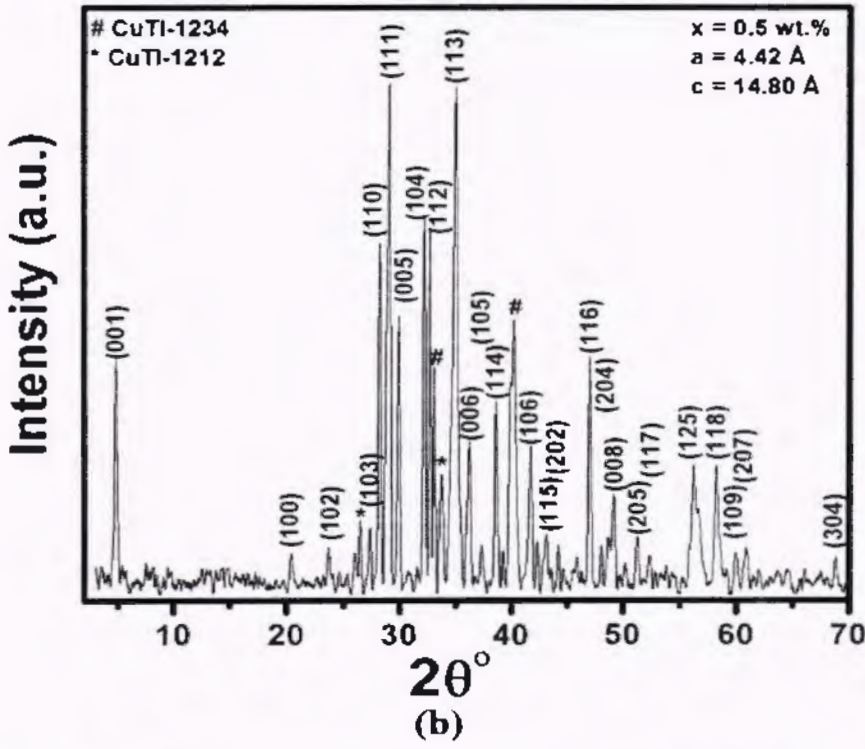


Fig 4.1: XRD pattern of MnFe_2O_4 nanoparticles.

The structure analysis of all $(\text{MnFe}_2\text{O}_4)_x/\text{CuTi-1223}$ composites was accomplished with the help of X-ray diffraction method (XRD). The majority of indexed peaks conformed as the tetragonal structure of CuTi-1223 phase through computerized check cell software according to (space group: P4/mmm). After analyzing all the acquired results, it was observed that the $(\text{MnFe}_2\text{O}_4)$ nanoparticles inclusion in host CuTi-1223 superconductor have very minute effects on its structure and stoichiometry. While some minor variation of both a and c, the cell parameters can be related to stress and strain produced as a result of these nanoparticles inclusion with in the host superconductor material.

In the (XRD) spectra of all composites, some shifting of well-indexed peaks towards higher angles is observed which most probably due to nanoparticles inclusion in host material. The un-indexed peaks are labeled with distinguishable sign to indicate the presence of some other impurities presence in our composites [2-6]. These impurities include CuTi-1212 and CuTi-1234 phases and some unknown impurities and labeled with different sing. The (XRD) spectra of all composites with various concentration are shown in Fig 4.2.





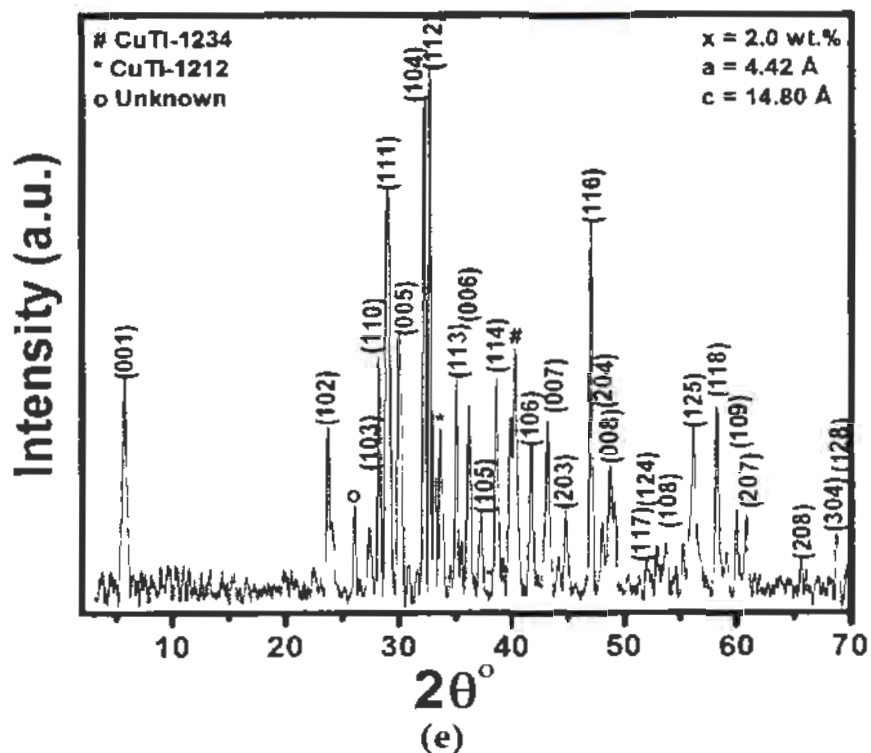
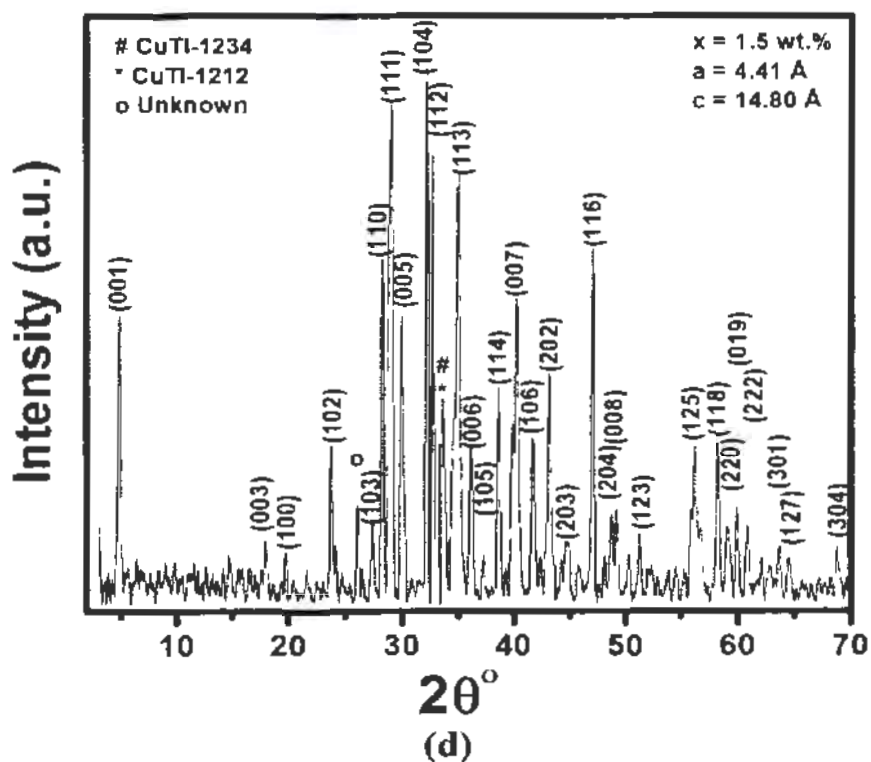
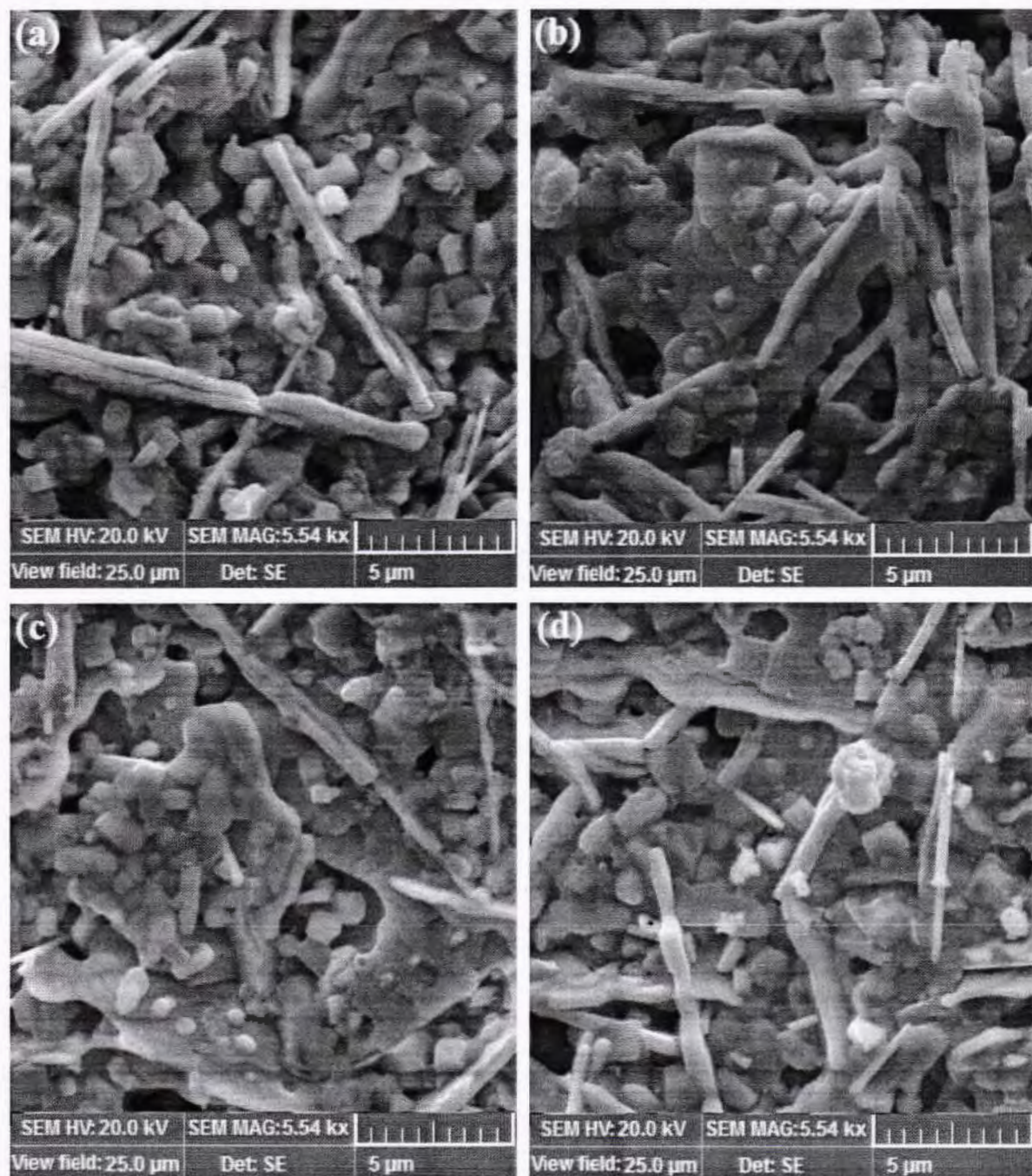


Fig 4.2: XRD of $(\text{MnFe}_2\text{O}_4)_x/\text{CuTi-1223}$ composites with (a) $x = 0$, (b) $x = 0.5$ wt. %, (c) $x = 1$ wt. %, (d) $x = 1.5$ wt. %, (e) $x = 2$ wt. %.

4.2 Scanning electron microscopy (SEM)

The surface features or surface morphology and distribution of added nanoparticles in superconductor matrix is briefly investigated by means of scanning electron microscopy (SEM) technique [2-7]. The SEM micrographs of $(\text{MnFe}_2\text{O}_4)_x/\text{CuTl-1223}$ superconductor composites are all shown in Fig. 4.3.



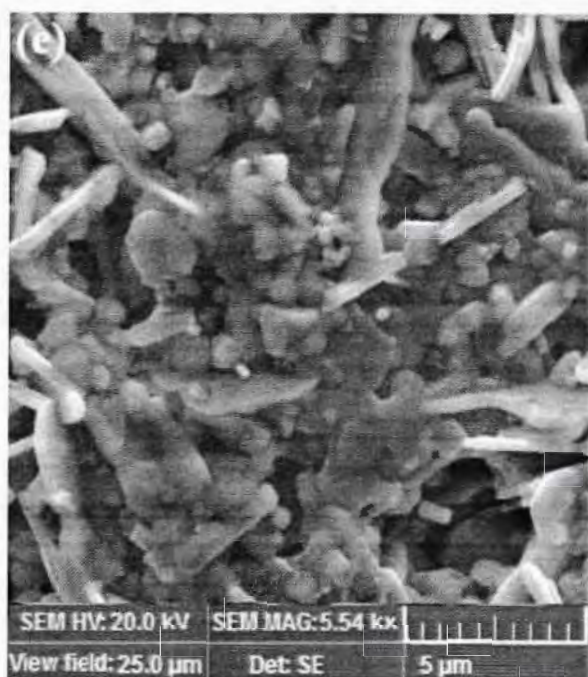


Fig 4.3: SEM of $(\text{MnFe}_2\text{O}_4)_x/\text{CuTi-1223}$ composites with (a) $x = 0$, (b) $x = 0.5$ wt. %, (c) $x = 1$ wt. %, (d) $x = 1.5$ wt. %, (e) $x = 2$ wt. %.

These micrographs clearly exhibit that, the MnFe_2O_4 nanoparticles inclusion in CuTi-1223 matrix improved its inter-grain connectivity. The density of void and pores reduced with increasing the MnFe_2O_4 nanoparticles concentration in host material. The higher concentration of these nanoparticles at interstitial spaces caused agglomeration at some areas and can be verified from above SEM results.

4.3 Energy dispersive X-rays spectroscopy

The results of EDX analysis are mostly used to conform the required elemental composition of given materials or compounds [8]. In our case, we performed the EDX analysis on both type of samples i.e. the samples with and without addition of MnFe_2O_4 nanoparticles. The EDX spectra of the sample with $x = 0$ wt. % concentration of nanoparticles shows no peak corresponds to other impurities or elements. While in the EDX spectra of the sample with $x = 0.5$ wt. % concentration of MnFe_2O_4 nanoparticles shows very small peaks corresponds to Fe and Mn among the other peaks of elements present in our composites. The EDX spectra of both samples are shown in Fig 4.4.

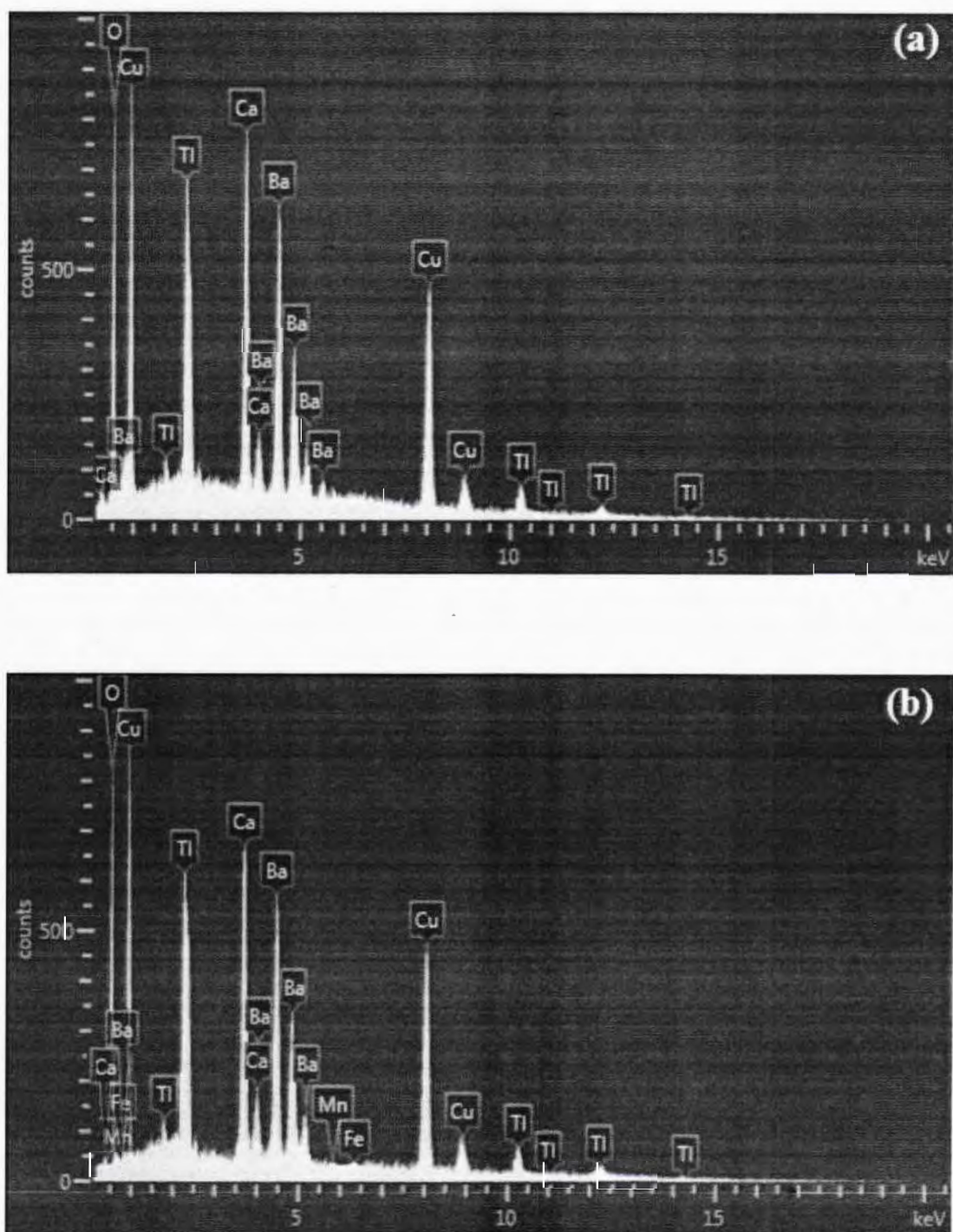


Fig 4.4: EDX spectra's of $(\text{MnFe}_2\text{O}_4)_x/\text{CuTi-1223}$ composites with (a) $x = 0$, (b) $x = 0.5$ wt. %.

4.4 Fourier transform infrared spectroscopy FTIR

The Fourier transform infrared spectroscopy (FTIR) is widely used as characterization tool to detect presence of various impurities within given material plus positions of various bands in the structure. FTIR absorption spectra of $(\text{MnFe}_2\text{O}_4)_x/\text{CuTi-1223}$ superconductor composites with various concentrations like ($x = 0, 0.5, 1.0, 1.5$ and 2.0 wt.%) in the range of (400 to 700 cm^{-1}) is shown in Fig. 4.5(b). The experimentally observed bands which are associated with apical oxygen atoms are located in range of (400 to 540 cm^{-1}), while bands in (541 to 600 cm^{-1}) are associated with planner oxygen atoms of CuO_2 planes. At last, the bands associated with O_δ atom are located between range of 670 to 700 cm^{-1} respectively [9]. In case of pure $\text{Cu}_{0.5}\text{Ti}_{0.5}\text{Ba}_2\text{Ca}_2\text{Cu}_3\text{O}_{10-\delta}$ samples, the apical oxygen modes of type $\text{Ti-O}_A\text{-Cu(2)}$, $\text{Cu(1)-O}_A\text{-Cu(2)}$ and $\text{Cu(2)-O}_P\text{-Cu(2)}$ planner oxygen mode were observed around 420 cm^{-1} , 459 cm^{-1} and 543 cm^{-1} respectively as shown in Fig. 4.5(a). After addition of $(\text{MnFe}_2\text{O}_4)$ nanoparticles, a slight variation in apical mode of type $\text{Ti-O}_A\text{-Cu(2)}$ is observed around 420 cm^{-1} to 418 cm^{-1} . The $\text{Cu(1)-O}_A\text{-Cu(2)}$ position almost remained unchanged in the range of $459\text{--}478\text{ cm}^{-1}$. The $\text{Cu(2)-O}_P\text{-Cu(2)}$ planner mode exhibits some variation around $543\text{--}545\text{ cm}^{-1}$. While on the other hand, the bands associated with O_δ remained unchanged around 669 cm^{-1} . The slight movement or variation in positions of different oxygen modes exhibits the presence of stress and strains in the materials, which definitely influences the bond lengths. However, all these observations conformed that, the oxygen vibrational phonon modes almost remained unaffected or simply unaltered after $(\text{MnFe}_2\text{O}_4)$ nanoparticles inclusion in CuTi-1223 matrix. This is the clear evidence that, $(\text{MnFe}_2\text{O}_4)$ nanoparticles did not substitute any atom of unit cell and adjusted or stayed at the grain boundaries of host CuTi-1223 superconductor.

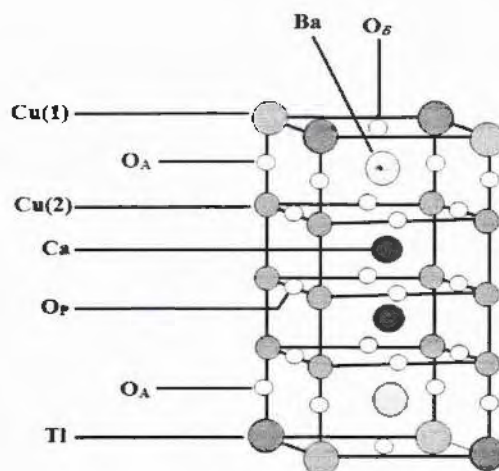


Fig. 4.5: (a) Unit cell of CuTi-1223

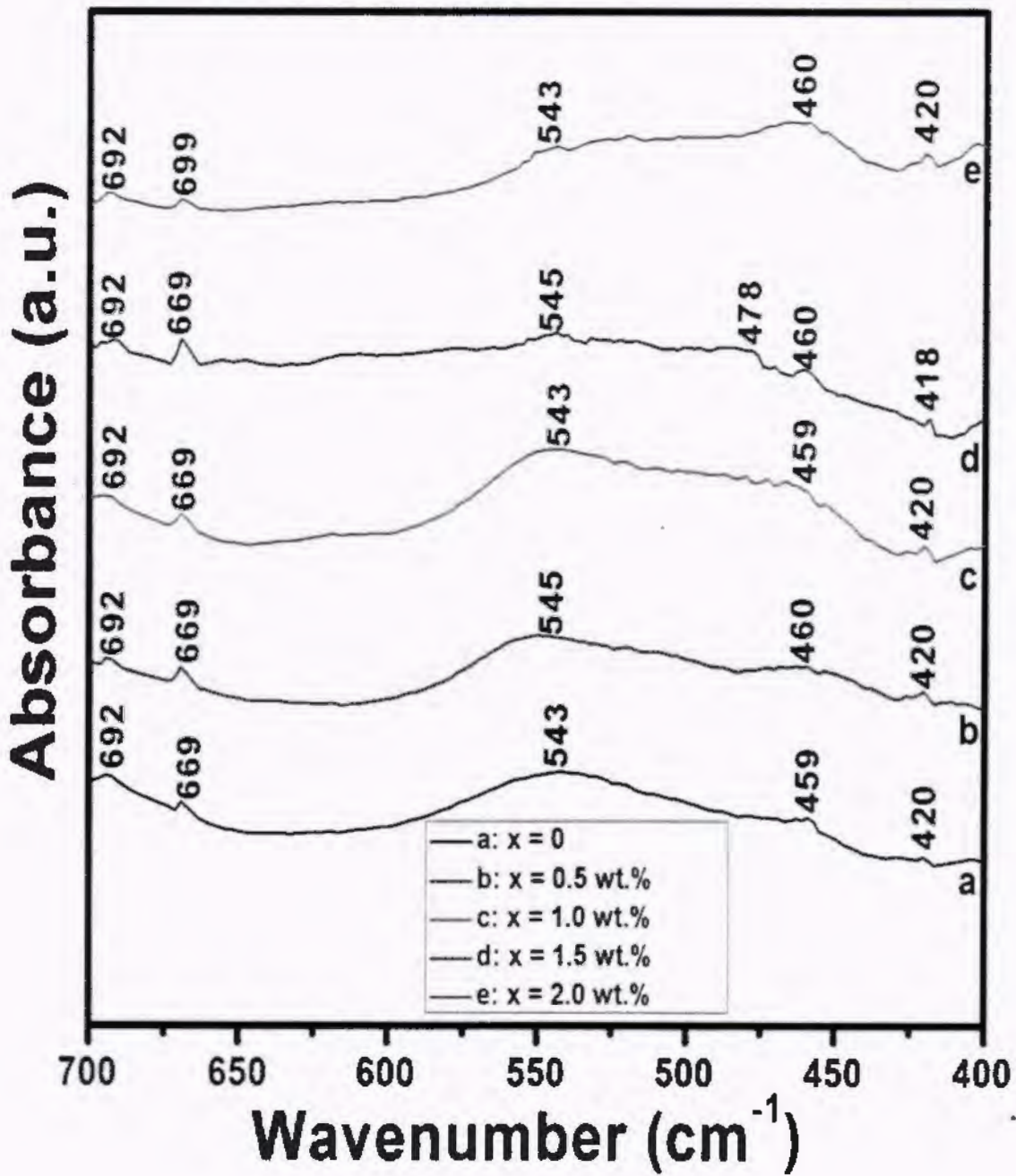


Fig. 4.5: (b) FTIR absorption spectra of $(\text{MnFe}_2\text{O}_4)_x/\text{CuTi-1223}$ superconductor composites with $x = 0, 0.5, 1.0, 1.5$ and $2.0 \text{ wt.}\%$.

4.5 Resistivity measurements

The dc-resistivity versus temperature measurements of $(\text{MnFe}_2\text{O}_4)_x/\text{CuTI-1223}$ superconductor composites added with various concentration of MnFe_2O_4 nanoparticles varied as ($x = 0, 0.5, 1.5$ and 2.0 wt.%) are shown in Fig.4.6. As we know that in superconductors with higher T_c , the resistive broadening is mainly due to critical temperatures of two types. One is defined as T_c^{onset} (K) at which formation of Cooper pair take place and second one is $T_c(0)$ at which given material transfer into bulk superconducting state. The value of T_c^{onset} (K) depends on material electronic properties while on other hand, value of $T_c(0)$ depends upon material micro-structural properties and the density of carriers in CuO_2 planes. The material tends to have lower $T_c(0)$ is most probably due presence of voids and weak inter-grain connectivity, as compared to another material with packed and well connected grains in spite of their equal T_c^{onset} (K) values [10-15].

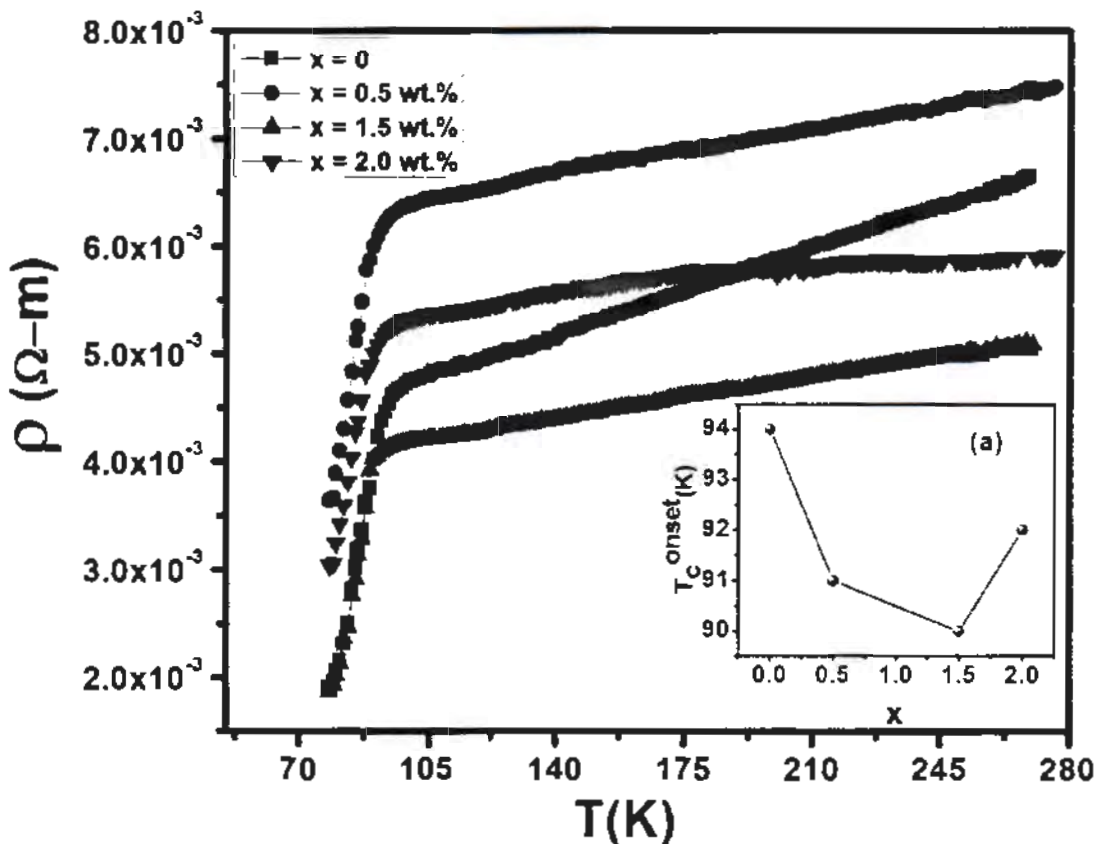


Fig. 4.6: Resistivity vs temperature measurements of $(\text{MnFe}_2\text{O}_4)_x/\text{CuTI-1223}$ superconductor composite with $x = 0, 0.5, 1.5$ and 2.0 wt. %. (a) variation in T_c^{onset} (K) verses x .

The measured values of T_c^{onset} (K) for the samples with added nanoparticles concentration of ($x = 0, 0.5, 1.5$ and 2.0 wt.%) are around 94 K, 91 K, 90 K and 92 K respectively as shown Fig.4.6(a). Here monotonically decreasing behavior of T_c^{onset} (K) is not surprising because these added nanoparticles are magnetic in nature and have an ability to suppress the overall superconductivity. Most vexing problem in these composites is the uniform and homogeneous distribution of MnFe_2O_4 nanoparticles at inter-grain boundaries of host CuTl-1223 superconductor. Therefore, the non-monotonic behavior or change in normal state resistivity of $(\text{MnFe}_2\text{O}_4)_x/\text{CuTl-1223}$ superconductor composites is most probably due to the inhomogeneous distribution of manganese ferrite nanoparticles at the grain-boundaries of the bulk materials.

Conclusion

We have successfully synthesized $(\text{MnFe}_2\text{O}_4)_x/\text{CuTi-1223}$ composites by adding manganese ferrite nanoparticles in CuTi-1223 superconducting matrix in different concentrations from $x = 0$ to $x = 2$ wt.%. XRD analysis of nanoparticles and superconductor matrix revealed the spinal and tetragonal structures, respectively. The calculated average crystallite size of MnFe_2O_4 nanoparticles by using Debye-Scherrer's formula was found equal to 20 nm. Results obtained from XRD and FTIR analysis both conformed that the inclusion of MnFe_2O_4 nanoparticles doesn't altered structure of our host CuTi-1223 phase. Improvement in grain size and reduction in pores and voids density were observed in SEM images, which shows the incorporation effects of MnFe_2O_4 nanoparticles between the grains of host CuTi-1223 phase. Overall decrease in T_c^{onset} (K) after inclusion of MnFe_2O_4 nanoparticles in CuTi-1223 phase is an expected evidence for having same decrease in $T_c(0)$ and magnitude of diamagnetism. This observed suppression in superconducting enhanced properties is most likely due to enhanced scattering of cooper pairs across magnetic (MnFe_2O_4) nanoparticles. The non-monotonic variation in both, normal state resistivity and superconducting properties of $(\text{MnFe}_2\text{O}_4)_x/\text{CuTi-1223}$ composites is most probably due to inhomogeneous distribution of (MnFe_2O_4) nanoparticles at the grain-boundaries of superconducting composites.

References

- [1] C. Giacovazzo, "Fundamentals of crystallography" Oxford University Press, (2002).
- [2] A. Jabbar, I. Qasim, S. A. Khan, K. Nadeem, M. Waqee-ur-Rehman, M. Mumtaz, and F. Zeb, "Highly coercive cobalt ferrite nanoparticles-CuTl-1223 superconductor composites" *J. Magn. Magn. Mater.* **377** (2015) 6.
- [3] M. Mumtaz, S. Naeem, K. Nadeem, F. Naeem, A. Jabbar, Y. R. Zheng, Nawazish A. Khan, and M. Imran, "Study of nano-sized $(\text{ZnFe}_2\text{O}_4)_y$ particles/CuTl-1223 superconductor composites" *Solid State Sci.* **22** (2013) 21.
- [4] Nawazish A. Khan, A. Saleem, and S. T. Hussain, "Enhanced inter-grain connectivity in nano-particles doped $(\text{Cu}_{0.5}\text{Tl}_{0.5})\text{Ba}_2\text{Ca}_2\text{Cu}_3\text{O}_{10-\delta}$ superconductors" *J. Supercond. Nov. Magn.* **25** (2012) 1725.
- [5] G. Hussain, A. Jabbar, I. Qasim, M. Mumtaz, K. Nadeem, M. Zubair, S. Q. Abbas, and A.A. Khurram, "Activation energy and excess conductivity analysis of $(\text{Ag})_x/\text{CuTl-1223}$ nanosuperconductor composites" *J. Appl. Phys.* **116** (2014) 103911.
- [6] K. Nadeem, G. Hussain, M. Mumtaz, A. Haider, and S. Ahmed, "Role of magnetic NiFe_2O_4 nanoparticles in CuTl-1223 superconductor." *Ceram. Int.* **10** (2015) 15041.
- [7] B. A. Albiss, I. M. Obaidat, M. Gharaibeh, H. Ghamlouche, and S. M. Obeidat, "Impact of addition of magnetic nanoparticles on vortex pinning and microstructure properties of Bi-Sr-Ca-Cu-O superconductor" *Solid State Commun.* **105** (2010) 1542.
- [8] C. Y. Huang, H. H. Tai, and M. K. Wu, "HIGH-FIELD AND MICROSTRUCTURE STUDIES OF SUPERCONDUCTING $n \text{YBa}_2\text{Cu}_3\text{O}_y$: AgO COMPOSITES." *Mod. Phys. Lett. B* **06** (1989) 525.
- [9] A. Jabbar, I. Qasim, K. M. Khan, Z. Ali, K. Nadeem, and M. Mumtaz, "Synthesis and superconducting properties of $(\text{Au})_x/\text{CuTl-1223}$ composites" *J. Alloys Compd.* **618** (2015) 110.
- [10] N. Novosel, D. Pajic, Z. Skoko, M. Mustapic, E. Babic, K. Zadro, and J. Horvat, "The Influence of CuFe_2O_4 Nanoparticles on Superconductivity of MgB_2 " *Phys. Procedia.* **36** (2012) 1498.
- [11] C. Ke, C. H. Cheng, Y. Yang, Y. Zhang, W. T. Wang, and Y. Zha, "Flux pinning behavior of MgB_2 doped with Fe and Fe_2O_3 nanowires" *Phys. Procedia.* **27** (2012) 40.

- [12] N. Novosel, and E. Babic, "Influence of magnetic nanoparticles on superconductivity of MgB_2 " *Physica C* **493** (2013) 119.
- [13] N. H. Mohammed, A. I. Abou Aly, R. Awad, I. H. Ibrahim, M. Roumie, and M. Rekaby, "Mechanical and electrical properties of $(\text{Cu}_{0.5}\text{Tl}_{0.5})$ -1223 phase added with nano- Fe_2O_3 " *J. Low. Temp. Phys.* **172** (2013) 234.
- [14] J.C. Zhang, F.Q. Liu, G.S. Cheng, J.X. Shang, J.Z. Liu, S.X. Cao, Z.X. Liu, *Phys. Lett. A* **201** (1995) 70.
- [15] P.F. Miceli, J.M. Tarascon, L.H. Greene, H.P. Barbou, F.J. Rotella, J.D. Jorgensen, *Phys. Rev. B* **37** (1988) 5932.